Monthly Notices
of the
ROYAL ASTRONOMICAL SOCIETY

Mon. Not. R. Astron. Soc. **422,** 521–541 (2012) doi:10.1111/j.1365-2966.2012.20628.x

The JCMT Legacy Survey of the Gould Belt: mapping ^{13}CO and C^{18}O in Orion A

J. V. Buckle,[1,2]★ C. J. Davis,[3] J. Di Francesco,[4,5] S. F. Graves,[1,2] D. Nutter,[6] J. S. Richer,[1,2] J. F. Roberts,[7] D. Ward-Thompson,[6] G. J. White,[8,9] C. Brunt,[10] H. M. Butner,[3,11] B. Cavanagh,[3] A. Chrysostomou,[3,12] E. I. Curtis,[1,2] A. Duarte-Cabral,[13,21,22] M. Etxaluze,[8,9] M. Fich,[14] P. Friberg,[3] R. Friesen,[4,5] G. A. Fuller,[13] J. S. Greaves,[15] J. Hatchell,[10] M. R. Hogerheijde,[16] D. Johnstone,[4,5] B. Matthews,[4] H. Matthews,[17] J. M. C. Rawlings,[18] S. Sadavoy,[4,5] R. J. Simpson,[19] N. F. H. Tothill,[10] Y. G. Tsamis,[20]‡ S. Viti,[18] J. G. A. Wouterloot[3] and J. Yates[18]

[1]*Astrophysics Group, Cavendish Laboratory, J J Thomson Avenue, Cambridge CB3 0HE*
[2]*Kavli Institute for Cosmology, c/o Institute of Astronomy, University of Cambridge, Madingley Road, Cambridge CB3 0HA*
[3]*Joint Astronomy Centre, 660 N. A'Ohoku Place, University Park, Hilo, HI 96720, USA*
[4]*National Research Council Canada, Herzberg Institute of Astrophysics, 5071 West Saanich Road, Victoria, BC V9E 2E7, Canada*
[5]*Department of Physics & Astronomy, University of Victoria, 3800 Finnerty Road, Victoria, BC V8P 5C2, Canada*
[6]*School of Physics & Astronomy, Cardiff University, 5 The Parade, Cardiff CF24 3AA*
[7]*Centro de Astrobiología (CSIC/INTA), Ctra de Torrejón a Ajalvir km 4, E-28850 Torrejón de Ardoz, Madrid, Spain*
[8]*Department of Physics and Astronomy, The Open University, Walton Hall, Milton Keynes MK7 6AA*
[9]*Science and Technology Facilities Council, Rutherford Appleton Laboratory, Chilton, Didcot OX11 0QX*
[10]*School of Physics, University of Exeter, Stocker Road, Exeter EX4 4QL*
[11]*Department of Physics and Astronomy, James Madison University, 901 Carrier Drive, Harrisonburg, VA 22807, USA*
[12]*School of Physics, Astronomy and Mathematics, University of Hertfordshire, College Lane, Hatfield AL10 9AB*
[13]*Jodrell Bank Centre for Astrophysics, School of Physics and Astronomy, The University of Manchester, Oxford Road, Manchester M13 9PL*
[14]*Department of Physics and Astronomy, University of Waterloo, Waterloo, ON N2L 3G1, Canada*
[15]*Scottish Universities Physics Alliance, Physics & Astronomy, University of St Andrews, North Haugh, St Andrews, Fife KY16 9SS*
[16]*Leiden Observatory, Leiden University, PO Box 9513, 2300 RA Leiden, the Netherlands*
[17]*National Research Council of Canada, Dominion Radio Astrophysical Observatory, 717 White Lake Road, Penticton, BC V2A 6J9, Canada*
[18]*Dept of Physics & Astronomy, University College London, Gower Street, London WC1E 6BT*
[19]*Oxford Astrophysics, Department of Physics, Denys Wilkinson Building, Keble Road, Oxford OX1 3RH*
[20]*Instituto de Astrofísica de Andalucía (CSIC), Camino Bajo de Huíor 50, 18008 Granada, Spain*
[21]*Univ. Bordeaux, LAB, UMR 5804, F-33270, Floirac, France*
[22]*CNRS, LAB, UMR 5804, F-33270, Floirac, France*

Accepted 2012 January 24. Received 2012 January 23; in original form 2010 October 25

ABSTRACT

The Gould Belt Legacy Survey will map star-forming regions within 500 pc, using Heterodyne Array Receiver Programme (HARP), Submillimetre Common-User Bolometer Array 2 (SCUBA-2) and Polarimeter 2 (POL-2) on the James Clerk Maxwell Telescope (JCMT). This paper describes HARP observations of the $J = 3 \rightarrow 2$ transitions of ^{13}CO and C^{18}O towards Orion A. The 15 arcsec resolution observations cover 5 pc of the Orion filament, including OMC 1 (including BN–KL and Orion bar), OMC 2/3 and OMC 4, and allow a comparative study of the molecular gas properties throughout the star-forming cloud. The filament shows a velocity gradient of $\sim$1 km s^{-1} pc^{-1} between OMC 1, 2 and 3, and high-velocity emission is detected in both isotopologues. The Orion Nebula and Bar have the largest masses and linewidths, and dominate the mass and energetics of the high-velocity material. Compact,

★E-mail: j.buckle@mrao.cam.ac.uk
‡Present address: European Southern Observatory, Karl-Schwarzschild-Str. 2, D-85748 Garching, Germany.

spatially resolved emission from CH_3CN, $^{13}CH_3OH$, SO, $HCOOCH_3$, CH_3CHO and CH_3OCHO is detected towards the Orion Hot Core. The cloud is warm, with a median excitation temperature of ∼24 K; the Orion Bar has the highest excitation temperature gas, at >80 K. The $C^{18}O$ excitation temperature correlates well with the dust temperature (to within 40 per cent). The $C^{18}O$ emission is optically thin, and the ^{13}CO emission is marginally optically thick; despite its high mass, OMC 1 shows the lowest opacities. A virial analysis indicates that Orion A is too massive for thermal or turbulent support, but is consistent with a model of a filamentary cloud that is threaded by helical magnetic fields. The variation of physical conditions across the cloud is reflected in the physical characteristics of the dust cores. We find similar core properties between starless and protostellar cores, but variations in core properties with position in the filament. The OMC 1 cores have the highest velocity dispersions and masses, followed by OMC 2/3 and OMC 4. The differing fragmentation of these cores may explain why OMC 1 has formed clusters of high-mass stars, whereas OMC 4 produces fewer, predominantly low-mass stars.

Key words: molecular data – stars: formation – ISM: kinematics and dynamics.

1 INTRODUCTION

1.1 The Gould Belt Legacy Survey

The James Clerk Maxwell Telescope (JCMT) Gould Belt Legacy Survey (hereafter GBS; Ward-Thompson et al. 2007) is a coordinated mapping survey of selected nearby star-forming regions in the Gould Belt using the JCMT. Most star formation within 500 pc of the Sun occurs in molecular clouds which are part of a larger structure named the Gould Belt. This is a ring-like collection of molecular clouds associated with a ring of OB associations, potentially with a common origin (Gould 1879; see also de Zeeuw et al. 1999; Pöppel 2001). The belt is approximately 700 pc in diameter, and the Sun is currently situated approximately 100 pc from the centre.

The GBS is mapping large portions of many of the nearby clouds to high sensitivity at 850 and 450 μm using the Submillimetre Common-User Bolometer Array 2 (SCUBA-2) camera (Holland et al. 2006). These data are being used to identify the pre-stellar and protostellar cloud populations. Somewhat smaller areas in a subset of Gould Belt clouds have also been mapped using Heterodyne Array Receiver Programme/Auto-Correlation Spectral Imaging System (HARP/ACSIS; Buckle et al. 2009) to observe the emission in three isotopologues of CO, to study the outflows and the kinematics of the dense gas. Finally, the SCUBA-2 Polarimeter (POL-2; Bastien, Jenness & Molnar 2005) will be used to measure the morphology of the magnetic field in the regions which have been mapped in both the submillimetre continuum and the CO isotopologues.

For the initial studies of other clouds in the Gould Belt mapped using HARP/ACSIS, see Buckle et al. (2010, Orion B); Davis et al. (2010, Taurus); Graves et al. (2010, Serpens) and White et al. (in preparation, Ophiuchus).

1.2 Orion A

The northern part of the Orion A giant molecular cloud – OMC 1, 2, 3 and, to the south of the Orion nebula, OMC 4 – has been the subject of considerable observational scrutiny (see the reviews of Bally 2008; O'Dell et al. 2008; Peterson & Megeath 2008). This region is often referred to as the 'S-shaped' or 'integral-shaped' filament (Bally et al. 1987; Johnstone & Bally 1999). The distance to the region has been measured, through the trigonometric parallax of stars within the Orion nebula cluster and through very long baseline interferometry observations of masers in the Orion Kleinman–Low (KL) region, to be 414 ± 7 pc (Menten et al. 2007) and 418 ± 6 pc (Kim et al. 2008), respectively. We use a distance of 415 pc in this work. Fig. 1 shows the combined United Kingdom Infrared Telescope (UKIRT) WFCAM/*Spitzer* IRAC image (Davis et al. 2009) of Orion A overlaid with the outline of the region observed in the GBS. Contours in ^{13}CO integrated emission and labels mark the regions described in more detail in this and following sections.

OMC 1, the peak in the filament [see, for example, the 350 μm observations of Lis et al. (1998) or the 450 and 850 μm maps of Johnstone & Bally (1999)], is centred behind the Trapezium cluster of hot young stars that illuminate the Orion nebula and photoionize the surrounding gas. The south-eastern edge of this ionized region is bounded by the 'Orion Bar' photon-dominated region (PDR). In addition to the massive OB stars that (together with a host of low-mass stars) constitute the Trapezium cluster, the Orion nebula also contains bright infrared (IR) sources, often referred to as the Becklin–Neugebauer (BN) and KL objects. The BN–KL region is roughly 1 arcmin north-west of the Trapezium cluster and is associated with the most intense molecular line emission region in the whole nebula (e.g. Beuther, Zhang & Greenhill 2005). The BN–KL region also coincides with the driving source of a powerful molecular outflow (Kwan & Scoville 1976). The flow is orientated along a north-west–south-east axis and exhibits a very wide opening angle. Near-IR images of the flow (in H_2 and [Fe II]) reveal a multitude of bullets or fingers that radiate outwards from the BN–KL region in almost all directions (see e.g. Allen & Burton 1993). The kinetic energy of this remarkable flow is of the order of 4×10^{40} J. Proper motion studies suggest that a single catastrophic event, occurring roughly 10^3 yr ago, has led to the outflow and associated molecular bullets (Allen & Burton 1993; Bally et al. 2011).

OMC 2 and 3, the regions directly to the north of the Orion nebula, contain many young, low-mass stars and associated molecular outflows and Herbig–Haro objects (Yu, Bally & Devine 1997; Yu et al. 2000; Stanke, McCaughrean & Zinnecker 2002; Williams, Plambeck & Heyer 2003; Davis et al. 2009). Indeed, it has been suggested that the ∼1700 young stars associated with OMC 1, 2 and 3 are part of the same complex, extending ∼3 pc from the Orion nebula (Peterson & Megeath 2008). Unlike OMC 1, the molecular gas traced by the structure of 8 μm emission in OMC 2/3 is largely seen in absorption against diffuse background nebula emission. Peterson & Megeath (2008) suggest these observations indicate the OMC 2/3 region contains protostars embedded in molecular

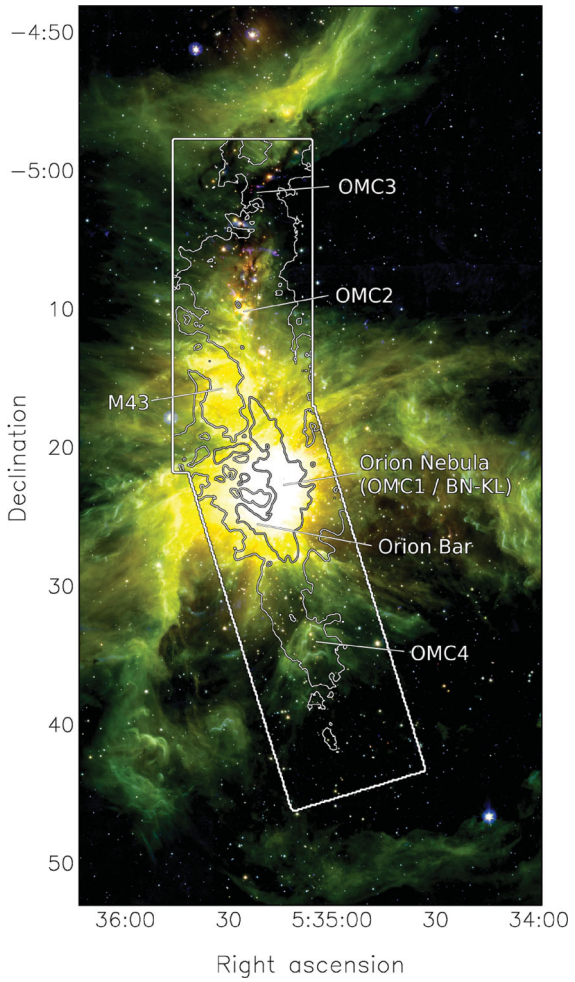

Figure 1. Combined UKIRT WFCAM/*Spitzer* IRAC image of Orion A (Davis et al. 2009), with the area observed by the GBS and described here shown by the solid rectangular contour. Regions discussed in the text are labelled. Sparse contours in ^{13}CO emission are used to highlight relevant regions.

filaments. Chini et al. (1997) present 1300 μm observations of OMC 2/3, revealing 21 compact sources; Davis et al. (2009) present similar 1200 μm observations, and find that many of these cores harbour outflow-driving protostars.

OMC 4 is a V-shaped group of molecular cores extending 10–15 arcmin south of OMC 1 (Johnstone & Bally 2006). The region is sparsely populated with young stars, though it does act as a bridge with the southern half of Orion A, the L 1641 molecular cloud which contains a far more widely distributed population of low-mass young stellar objects (YSOs) and protostars.

Low-resolution, wide-field CO and ^{13}CO observations of OMC 1/2/3 have been presented by a number of groups (e.g. Kutner et al. 1977; Maddalena et al. 1986; Bally et al. 1987; White & Sandell 1995; Wilson et al. 2005). These data roughly trace the dust filament seen in (sub)millimetre continuum emission, and indicate a north-to-south local standard of rest velocity shift from ∼12 to 4 km s^{-1}. HCN, CI, CS and C^{18}O observations of OMC 1 have been presented by White & Padman (1991), Bergin, Snell & Goldsmith (1996) and Goldsmith Bergin & Lis (1997), while Tatematsu et al. (2008) present recent N_2H^+ and HC_3N observations. Finally, high-resolution NH_3 maps of OMC 1 and 2 reveal remarkable molecular filaments radiating northwards from the Orion nebula (Wiseman & Ho 1998). These filaments have a similar structure to the molecular bullets observed in the near-IR and, on a larger scale, the radial filaments seen in SCUBA 850 μm dust emission (Johnstone & Bally 1999), although the locations and scales are different.

1.2.1 Outline

This paper presents a first look at the complete GBS HARP/ACSIS survey data for the dense filament in Orion A. The filament was mapped using the $J = 3 \rightarrow 2$ transition of ^{13}CO and C^{18}O. Observations of this region in the ^{12}CO $J = 3 \rightarrow 2$ transition, which will be incorporated into the survey data, are described elsewhere (Graves et al., in preparation). The ^{13}CO and C^{18}O lines were mapped with a velocity resolution of 0.05 km s^{-1} in order to study the kinematic state of the gas and investigate the support mechanisms of the pre-stellar cores, and to study the role of turbulence in the formation of the cores. Section 2 describes the observations and data reduction, while Section 3 presents an overview of the reduced data sets including, in Section 3.6, the rich molecular spectrum in the region surrounding OMC 1. In Section 4, we calculate and discuss the overall physical characteristics and kinematics of the cloud. In Section 5, we use C^{18}O emission to investigate the properties of dense cores detected by SCUBA. Our findings are summarized in Section 6.

2 OBSERVATIONS AND DATA REDUCTION

The observations presented here comprise 34.2 h of data taken over several nights from 2009 February to 2010 October using HARP/ACSIS on the JCMT. The $J = 3 \rightarrow 2$ transitions for the isotopologues are at frequencies of 330.540 GHz (^{13}CO) and 329.278 GHz (C^{18}O), which can be observed simultaneously using HARP/ACSIS. The system temperatures, which are measured for each detector in every observation, varied from 225 to 689 K for atmospheric opacities of 0.03–0.07[1] in the ^{13}CO data, with median system temperature of 327 K. Two overlapping fields covering Orion A (see Fig. 1) are analysed: (i) the OMC 2/3 filament, (8.5 × 23.3) arcmin^2 centred on $05^h35^m25^s.0$, $-05^\circ10'22''$ (J2000) at PA = 0° (east of north) and (ii) the OMC 1/4 filament, (8.4 × 25) arcmin^2, centred on $05^h35^m06^s.0$, $-05^\circ32'55''$ (J2000) angled at PA = +16°.

The same absolute off-position was used for both fields: $05^h35^m14^s$, $-04^\circ47'32''$. This was verified to be absent of emission by examining a short 60 s position-switched 'stare' observation in ^{12}CO $J = 3 \rightarrow 2$.

The data were reduced using the STARLINK project ORAC-DR pipeline software,[2] with KAPPA (Currie et al. 2008) routines used to mask out poorly performing detectors and calculate a self-flat (see Curtis, Richer & Buckle 2010) for each observation. SMURF (Jenness et al. 2008) routines were used to make the cube using a Gaussian gridding technique, with 6 arcsec pixels and an 8 arcsec full width at half-maximum (FWHM) Gaussian, giving an effective angular resolution of 17.3 arcsec in the final data cubes. These data are presented as a 'first look' at the data being gathered for the GBS towards Orion. HARP data acquisition towards the regions in the Gould Belt survey is complete, and the final data sets and quality-assessed data products will be released after all the data are reduced

[1] Opacity measured from Caltech Submillimeter Observatory tau at 225 GHz.
[2] http://starlink.jach.hawaii.edu/starlink

Table 1. Mean noise levels of GBS Orion A data.[a]

Source	Mean 1σ rms K^{-1}	
	^{13}CO	C^{18}O
Northern filament	0.24	0.28
Southern filament	0.16	0.19

[a]6 arcsec pixels, 17.3 arcsec beam, 0.1 km s^{-1} channels.

using the Gould Belt ORAC-DR pipeline, currently in development. Future papers will describe inter-region comparisons using the final data sets. Table 1 describes the mean noise achieved in the 'first look' data cubes in Orion A.

Data are presented in units of antenna temperature (T_A^*; Kutner & Ulich 1981), which can be converted to main beam temperature (T_{mb}) using $T_{mb} = T_A^*/\eta_{mb}$. For these data, we adopt a value of $\eta_{mb} = 0.61$ (Buckle et al. 2009). NGC 2071-IR was observed as a calibration source for each observation, with flux calibration accuracy estimated to be 20 per cent. Pointing was regularly checked using JCMT standard sources before and after observations, the largest pointing shift being 4 arcsec, with median offset 2 arcsec.

3 RESULTS

Fig. 2 shows the ^{13}CO and C^{18}O total integrated intensity maps of Orion A, both of which trace the integral-shaped filament. The data have been scaled to highlight the extent of emission, and have peak integrated intensities of 666 K km s^{-1}(^{13}CO) and 102 K km s^{-1}(C^{18}O). The ^{13}CO data are integrated over the velocity range from −35 to 50 km s^{-1}, with OMC 1 containing the most high-velocity emission. The C^{18}O data are integrated over the velocity range from –15 to 25 km s^{-1}. Fig. 3 shows a position velocity (PV) diagram tracing the entire Orion A filament from north to south (the direction of the slice is shown in Fig. 2). There are a number of features present in these data. Although the PV slice only samples a narrow spatial slice of the whole filament, a large number of outflows are seen (labelled in Fig. 3) as emission redshifted and blueshifted to high velocity with respect to the main filament. There is a high-velocity cloud marked, which is not contiguous in velocity with the main filament. There is a general gradient in velocity along the length of the Orion A filament, with OMC 3 to the north at a velocity of ∼11 km s^{-1}and OMC 4 to the south at around ∼8 km s^{-1}. This gradient is fairly monotonic, ∼1 km s^{-1} pc^{-1}, until the OMC 4 region. South of the OMC 4 region, the gradient reverses trend, and we describe this region in more detail in Section 3.5. There is a sharp deviation in the trend with a region at declination −5°31′00″ (in between the OMC 1 and OMC 4 material) at a much higher velocity than its surroundings.

In the C^{18}O data, the small-scale features to the north (near OMC 2 and OMC 3) are approximately the same brightness as the region near OMC 1 (note that the Orion A PV slice in Fig. 3 does not pass

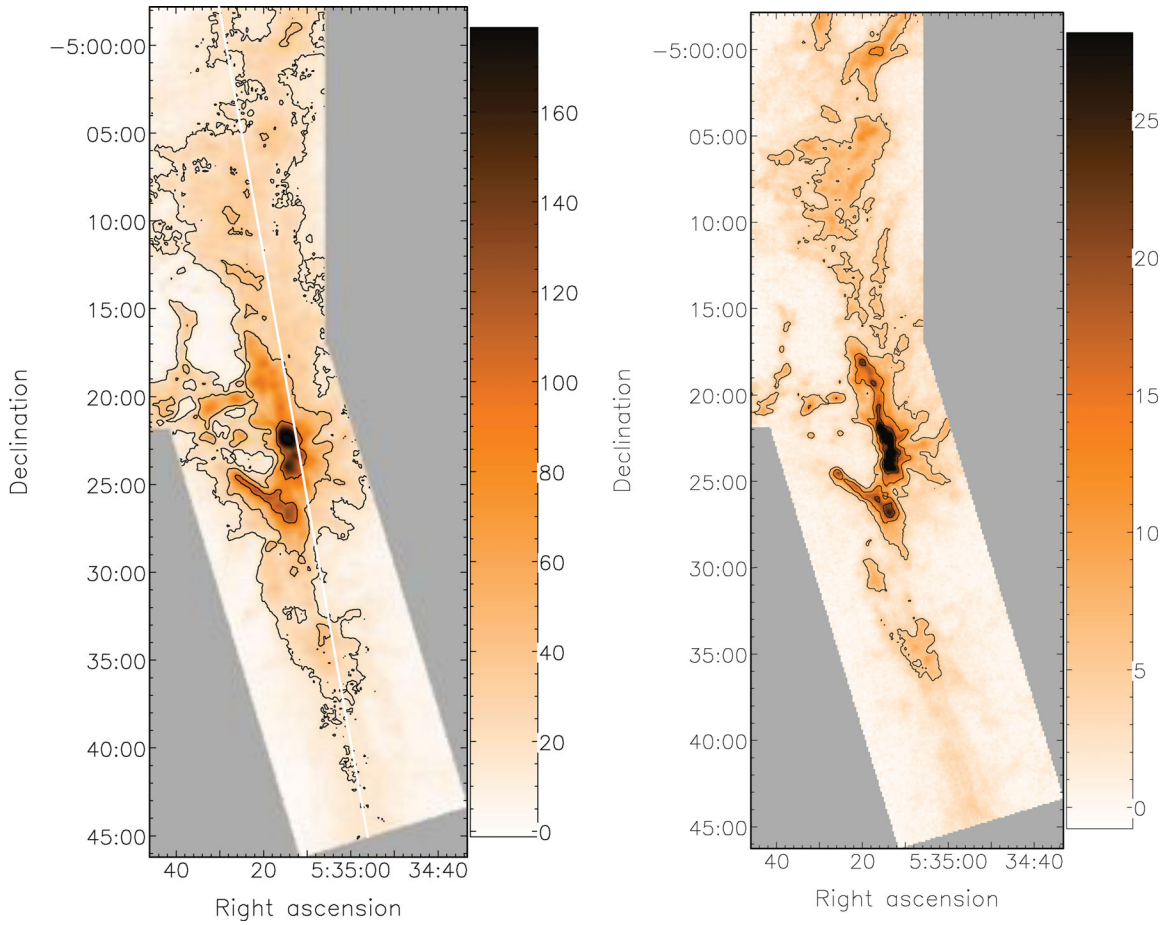

Figure 2. Orion A integrated intensity maps, with the colour scale showing integrated values in K km s^{-1}. Left: ^{13}CO, integrated from –35 to 50 km s^{-1}, with contour levels at 18, 40, 100, 300 K km s^{-1}. The white line shows the direction of the PV slice extracted for Fig. 3. Right: C^{18}O integrated from −10.0 to 25.0 km s^{-1}, with contour levels at 5, 12, 20 K km s^{-1}.

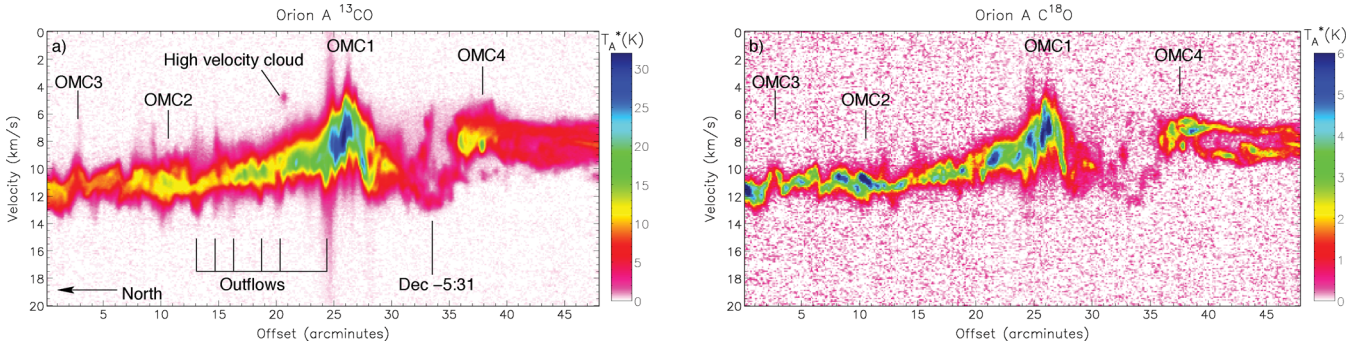

Figure 3. PV diagrams showing a cut through the entire Orion A filament from north to south with the (a) ^{13}CO and (b) C^{18}O molecular tracers. The PV slice runs from $5^h35^m30\overset{s}{.}4$, $-4°56'55''$ to $5^h34^m55\overset{s}{.}1$, $-5°46'13''$ (J2000), as shown in Fig. 2.

over the peak of OMC 1), whereas the same features in the ^{13}CO data are significantly fainter than those towards OMC 1, indicating that there may be significant opacity effects towards OMC 1. The velocity structure near declination $-5°31'$ shows a break in emission, which suggests that OMC 4 may be physically detached from OMC 1/2/3. We describe in more detail individual regions of the data in the following sections.

3.1 OMC 1

The emission is brightest towards OMC 1, where integrated intensities reach $>600\,\mathrm{K\,km\,s^{-1}}$ in ^{13}CO, and the line profiles of both isotopologues are extremely broad. The spectra shown in Fig. 4 are taken from a single pixel at $5^h35^m14\overset{s}{.}6$, $-5°22'28''$ (J2000), which has the highest C^{18}O integrated intensity of $91\,\mathrm{K\,km\,s^{-1}}$, and where very broad line wings are seen in both isotopologues. In the near-IR, the molecular hydrogen line profiles associated with the Orion bullets are particularly broad (Tedds, Brand & Burton 1999), consistent with the very broad ^{13}CO and C^{18}O profiles we observe in this region. These bullets are presumably driving shocks, and entraining even the densest gas in the OMC 1 core. In the spectra immediately surrounding the OMC 1 core (also known as the Orion A hot core), we detect several molecular lines, which are described further in Section 3.6.

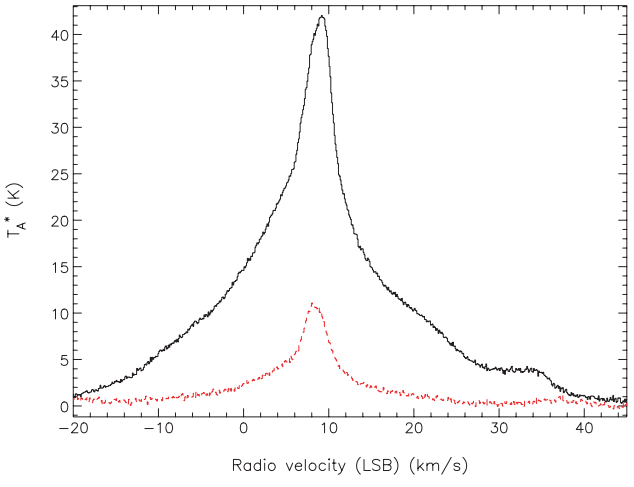

Figure 4. ^{13}CO spectrum (solid line) and C^{18}O spectrum (dashed line) taken from a single position at the peak of the C^{18}O integrated intensity, $5^h35^m14\overset{s}{.}6$, $-5°22'28''$ (J2000), towards OMC 1.

Both CO isotopologues display a wealth of filaments and arcs at several velocity intervals throughout the mapped region. Extending from OMC 1, we see structures similar in direction and length to the dense fingers first detected by Wiseman & Ho (1998) in NH_3. These filamentary features are most clearly seen in individual channel maps. Fig. 5 shows the C^{18}O channel maps from 6.9 to 9.0 km s^{-1}, in 0.5 km s^{-1} velocity intervals. Radial fingers can be seen to expand from OMC 1 as the velocity increases from 6 to 10 km s^{-1}. The fingers are most clearly defined, and have a maximum spatial extent, at $\sim$8 km s^{-1}. They are on a larger spatial scale and not aligned with the high-velocity HH bullets that have been detected in this region (Tedds et al. 1999; Takami et al. 2002). Squares in Fig. 5 mark the positions of the HH bullets. In the central regions, the HH bullets extend in generally the same directions as the C^{18}O fingers. The bullets to the north lie between the fingers of emission that we see in C^{18}O. A careful comparison of our channel maps with an H_2 image of the region does not indicate an obvious causal relationship between the two phenomena. The ^{13}CO also shows the same structure across these velocity channels.

Fig. 6 shows a PV diagram centred on the main outflow source in OMC 1. This shows that whilst the high-velocity material (less than 2 km s^{-1} and greater than 16 km s^{-1}) is spatially coincident, the lower velocity material at the base of the outflow (4–6 and 13–15 km s^{-1}) is offset by 12 arcsec. The emission from the region around the outflow source itself shows a strong localized gradient in velocity as function of position. The CO outflow is marginally resolved spatially. The extension to the south-east seen in Fig. 6(c) is consistent with the east–west asymmetry as seen in the interferometric data CO $J = 1$–0 of Chernin & Wright (1996).

3.2 Orion bar

The Orion bar, after the OMC 1 core, is the second most prominent emission feature in both isotopologues. The bar is centred at a velocity of 10 km s^{-1}, with a slight velocity gradient along its length. There are no outflows, and very little fragmentation is visible along the bar. Fig. 7(a) shows CO spectra from the northern extent of the Orion bar, at $5^h35^m23\overset{s}{.}8$, $-5°25'16''$. Both spectra show a slight asymmetry, with emission in the redshifted line wing stronger than in the blueshifted wing. The spectra from the Orion bar are considerably narrower than is seen towards the central region of OMC 1 (Fig. 4).

Fig. 7(b) shows the ^{13}CO and C^{18}O intensity contours overlaid on the SCUBA 850 μm map (Nutter & Ward-Thompson 2007). The bar appears slightly different in the isotopologues of CO and the submillimetre continuum. When viewed with C^{18}O, the bar

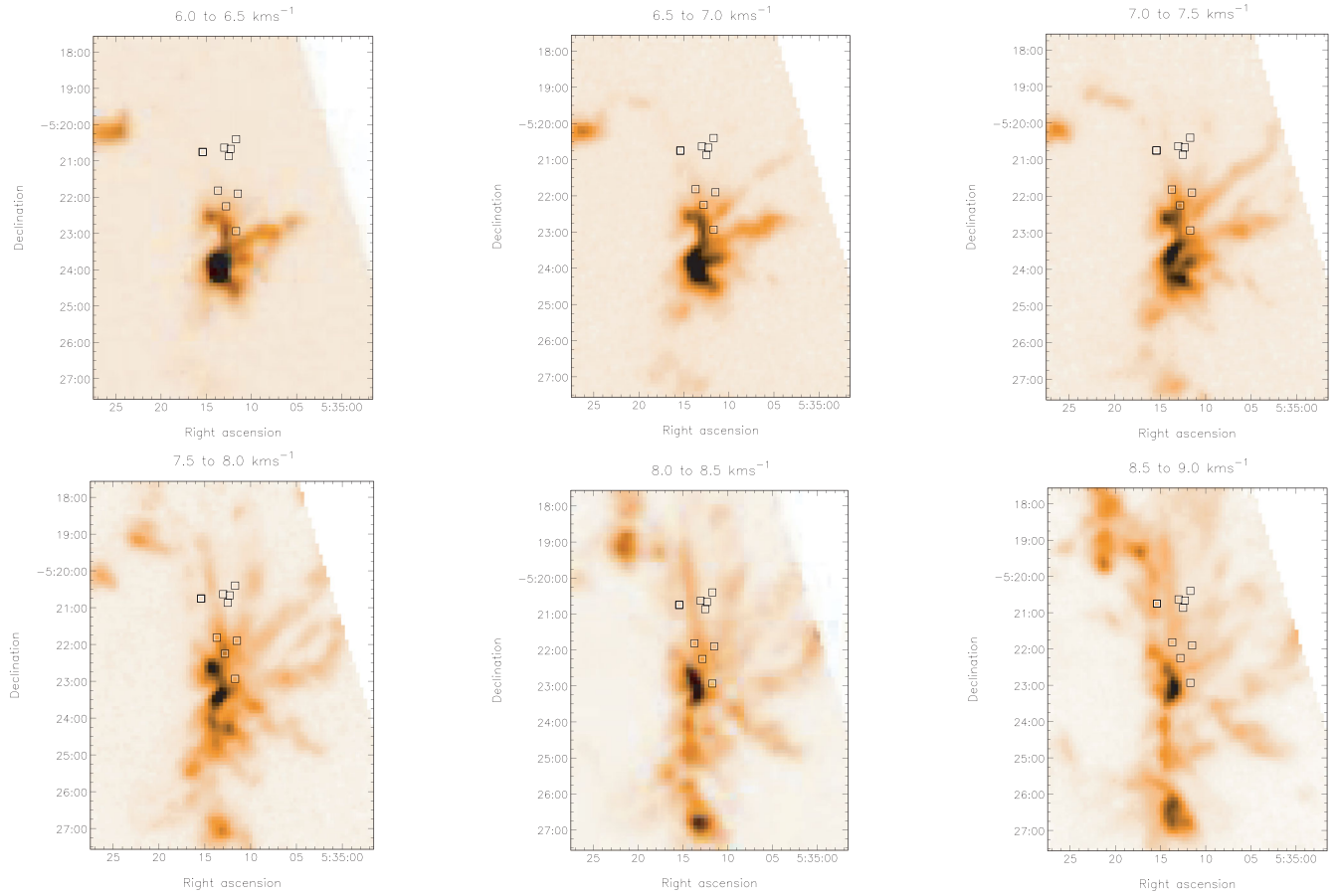

Figure 5. C^{18}O channel maps of integrated intensity from 6.0 to 9.0 km s^{-1}, in 0.5 km s^{-1} velocity intervals, showing the fingers radiating from OMC 1. Velocity intervals are marked on the plots, and squares mark the positions of HH bullets (Takami et al. 2002).

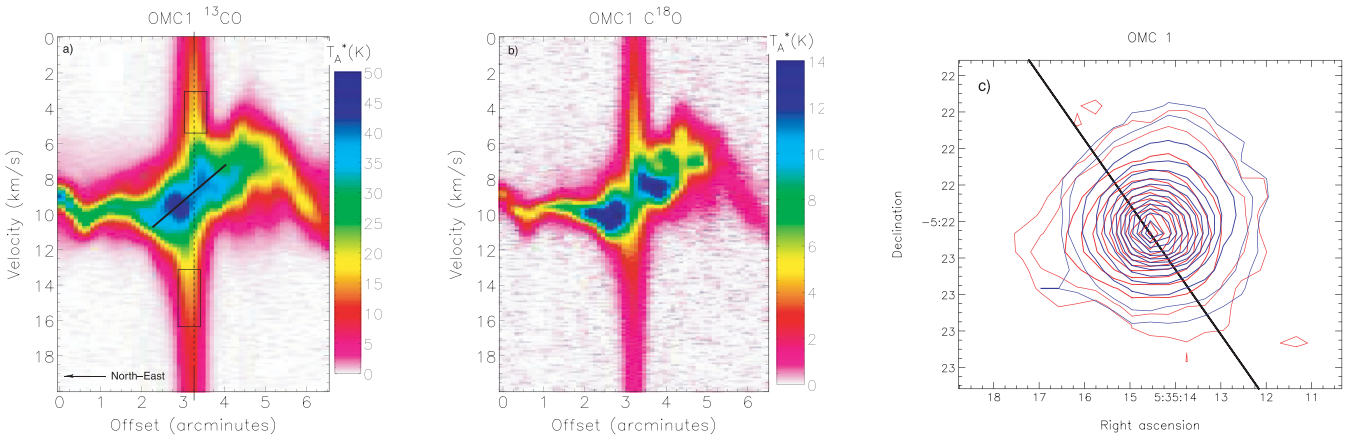

Figure 6. PV diagrams through OMC 1, showing (a) the ^{13}CO and (b) C^{18}O molecular tracers. The vertical black lines highlight the consistent position of the high-velocity portion of the outflow. The black boxes illustrate the difference in position of the inner parts of the outflow. (c) ^{13}CO emission in the blue (−20 to −5 km s^{-1}) and red (+25 to +45 km s^{-1}) line wings, with contours at 1, 2, 5, 10 K km s^{-1} (and incrementing by 5 K km s^{-1}). The black line indicates the location of the PV slice, which runs from $5^h35^m22^s.0$, $-5°19'49''$ to $5^h35^m07^s.1$, $-5°25'07''$(J2000).

is narrower and appears to peak slightly further away from OMC 1, to the outside of the H II region. The submillimetre continuum emission is stronger on the inside of the bar. Johnstone & Bally (1999) note that the bar is seen at longer wavelengths to break up into two parallel ridges, with the inner part illuminated by free–free emission.

3.3 Orion M43 reflection nebula

The M43 reflection nebula can be seen in Fig. 2 as a distinctive cavity centred at $5^h35^m33^s$, $-5°16'00''$, with very little emission across the two isotopologues. The PV diagram (Fig. 8) across the cavity at a declination of $-5°16'00''$ shows the velocity field around

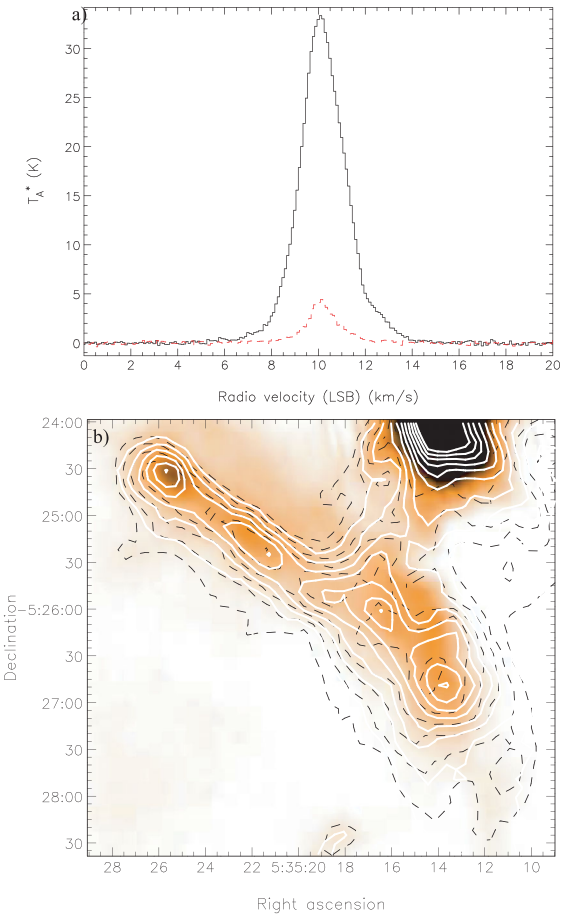

Figure 7. (a) ^{13}CO spectrum (solid line) and C^{18}O spectrum (red dashed line) taken from a single position at the northern end of the Orion bar, $5^h35^m23^s.8$, $-5°25'16''$ (J2000). (b) ^{13}CO (black dashed contours, from 50 K km s^{-1} in steps of 15 K km s^{-1}) and C^{18}O (white solid contours, from 5 K km s^{-1} in steps of 3 K km s^{-1}) intensity contours overlaid on the SCUBA 850 μm map (Nutter & Ward-Thompson 2007) of the Orion bar.

this region. The western wall of the cavity shows a slight velocity gradient, following the overall velocity gradient along the Orion A filament. The eastern wall of the cavity shows a sharp spatial cut-off across the velocity range. The few isolated cores within the cavity lie at the same velocity as the adjacent part of the wall and thus appear to be following the same velocity gradient.

3.4 OMC 2/3

Most of the ongoing star formation in OMC 2/3 is to the west and north of M43. OMC 2 shows a number of outflows and a faint high-velocity cloud at 13.5 km s^{-1} (Fig. 3). We do not see a large velocity gradient across OMC 2. OMC 3 is seen as a narrow filament in the submillimetre continuum with a number of small-scale structures (see Figs 9a–c). The emission from ^{13}CO is seen to be from a much broader region to the north of the 850 μm filament, with a number of structures extending away from the continuum emission. The strongest of these can be seen at the position $5^h35^m23^s$, $-5°00'05''$, with further clumps and arcs to the east and the south. The C^{18}O emission (not shown) more closely follows the continuum emission, but like the ^{13}CO, is only bright in the northern portion of the continuum filament.

There is much less similarity between both isotopologues and the continuum data in the southern part of the filament. The continuum emission shows a concentrated filament, which is absent of embedded sources, while the integrated intensity maps of ^{13}CO and C^{18}O show a fairly flat emission structure along the filament, with no embedded peaks or regions of higher emission.

The OMC 3 region is investigated in more detail in Figs 9(b) and (c), which shows a PV slice along the southern part of the continuum filament (location shown as a blue line in Fig. 9a). This shows that while there is very little material seen in the integrated intensity map (Fig. 9a), there is a small amount of material present, limited to the central velocity of the filament. There are no outflows along this portion of the filament, although they can be seen at either end of this filament, where the embedded sources are seen in both the continuum and the isotopologues.

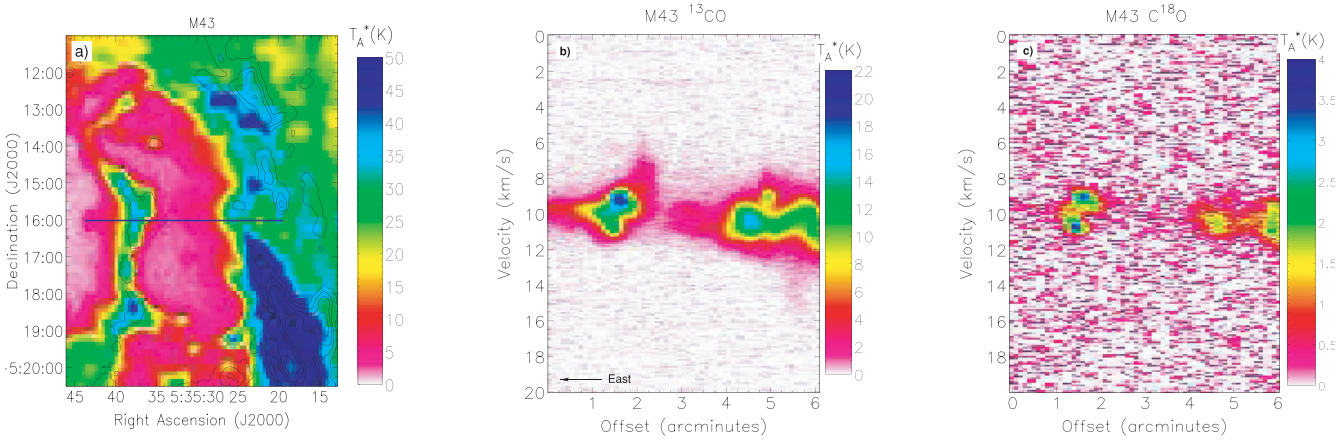

Figure 8. (a) ^{13}CO integrated intensity map of M43, with 850 μm continuum data from SCUBA overlaid as contours. The blue line shows the location of the PV slice. The PV diagrams across the M43 reflection nebula show the (b) ^{13}CO and (c) C^{18}O molecular tracers. The PV slice runs from $5^h35^m43^s.7$, $-5°16'01''$ to $5^h35^m19^s.6$, $-5°16'01''$(J2000).

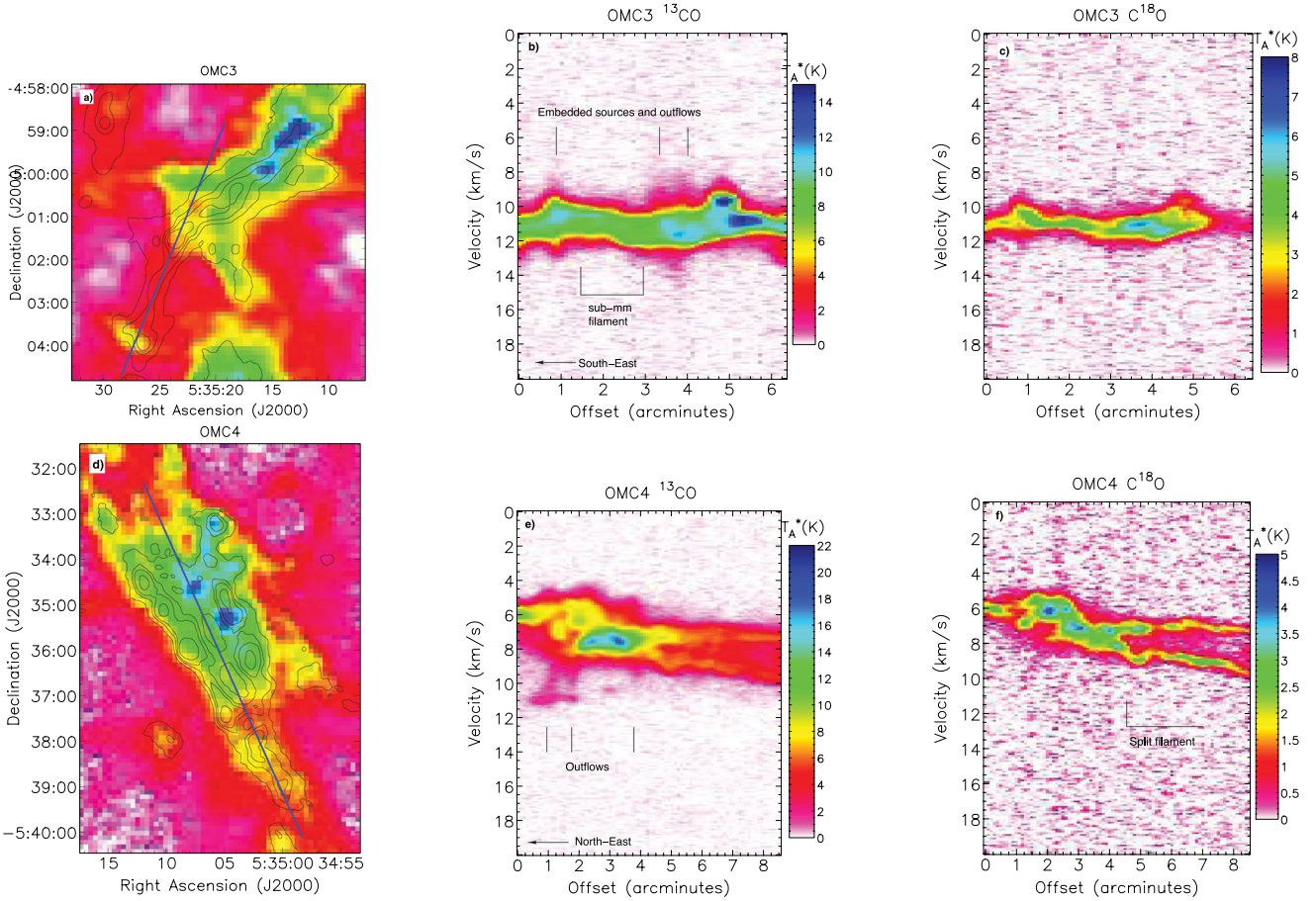

Figure 9. (a) ^{13}CO integrated intensity map of the OMC 3 region, with 850 μm continuum data from SCUBA overlaid as contours. Contour levels are 0.1, 0.5, 1 and 2 Jy beam^{-1}. The blue line shows the location of the PV slice, which runs from south to north. The PV diagrams of the southern portion of OMC 3 show the (b) ^{13}CO and (c) C^{18}O molecular tracers. (d) C^{18}O integrated intensity map of the OMC 4 region, with 850 μm continuum data from SCUBA overlaid as contours. Contour levels are 0.05, 0.2, 0.3 and 0.5 Jy beam^{-1}. The blue line shows the location of the PV slice, which runs from north to south. The PV diagrams of OMC 4 show the (e) ^{13}CO and (f) C^{18}O molecular tracers.

3.5 OMC 4

OMC 4 is seen as two separate filaments in the submillimetre continuum in the shape of a 'V', as shown in Fig. 9(d). The C^{18}O emission from OMC 4 matches the submillimetre continuum fairly well, though the western filament is brighter than the eastern one. The dip between the two filaments to the north is not very pronounced, unlike the structure seen in submillimetre continuum. The velocity difference between the two components of the western filament increases to the south, in contrast to the spatial distance between the two submillimetre filaments, which increases to the north. The ^{13}CO shows less similarity to the overall morphology of the submillimetre continuum emission, with very little emission from the eastern filament. PV maps along OMC 4 are shown in Fig. 9(e) and (f). The whole filament is found at velocities of 6–10 km s^{-1}, in agreement with the overall velocity gradient of Orion A. However, the general trend within OMC 4 is opposite to that in the region as a whole. At its southern end, the filament splits into two components along the line of sight, separated by ∼2 km s^{-1}. This is much more pronounced in the C^{18}O than in the ^{13}CO, as shown in Fig. 10.

There are three identified outflows, although these are not centred on the brightest sources in the filament, but trace back to some fainter sources which are seen in the submillimetre continuum.

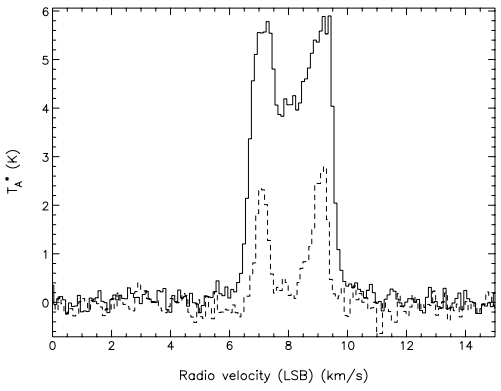

Figure 10. ^{13}CO spectrum (solid line) and C^{18}O spectrum (dashed line) taken from a single position in OMC 4, 5^{h}35^{m}00^s.8, −5°38′40″ (J2000).

3.6 Other lines

In addition to the ^{13}CO and C^{18}O lines that are the focus of this paper, the Orion region contains many rich molecular cores with a plethora of other astrochemical lines. The most spectacular of these molecular cores is the OMC 1 core (the Orion A hot core), which has been the focus of many spectral line surveys. The astrochemistry

of this has been studied by many authors: 72–91 GHz (Johansson et al. 1984), 70–115 GHz (Turner 1989), 80–115, 130–178 and 197–281 GHz (Tercero et al. 2010), 138–151 GHz (Lee, Cho & Lee 2001), 150–160 GHz (Ziurys & McGonagle 1993), 215–247 GHz (Sutton et al. 1985), 216–242 GHz (Blake et al. 1986), 247–263 GHz (Blake et al. 1987), 257–273 GHz (Greaves & White 1991), 260–328 GHz (Yoshida & Phillips 2005), 330–360 GHz (Jewell et al. 1989), 325–360 GHz (Schilke et al. 1997), 342–359 GHz (White et al. 1986), 334–343 GHz (Sutton et al. 1995), 607–725 GHz (Schilke et al. 2001), 780–903 GHz (Comito et al. 2005), 190–900 GHz (Serabyn & Weisstein 1995), 44–188 μm by Lerate et al. (2006), 486–492 and 541–577 GHz by Olofsson et al. (2007) and Persson et al. (2007), and 42.3–43.6 GHz (Goddi et al. 2009). The molecular lines dominate the submillimetre continuum emission towards the peak sources (Serabyn & Weisstein 1995; Johnstone & Bally 1999). We have examined the two spectral windows observed in this survey (centred on the ^{13}CO and C^{18}O lines) to look at the spatial distributions of any other lines that are present. The central-pixel spectra for both receiver tunings are shown in Fig. 11.

The central spectrum is rich in molecular lines towards the OMC 1 core, containing strong lines of ^{13}CO, C^{18}O, CH_3CN, $^{13}CH_3OH$ and SO, as well as weaker lines of CH_3CHO, HC_3HO, CH_3OCHO and H_2C_3HCN. In addition we also confirm three previously reported unidentified lines. Some of these lines show the characteristic broad emission from the well-known outflow source. Although we cannot be certain of the identification of all these weak lines due to the crowded and confused spectrum, the most likely carrier has been chosen, based on the presence of other transitions of the carrier, and their upper state energy levels.

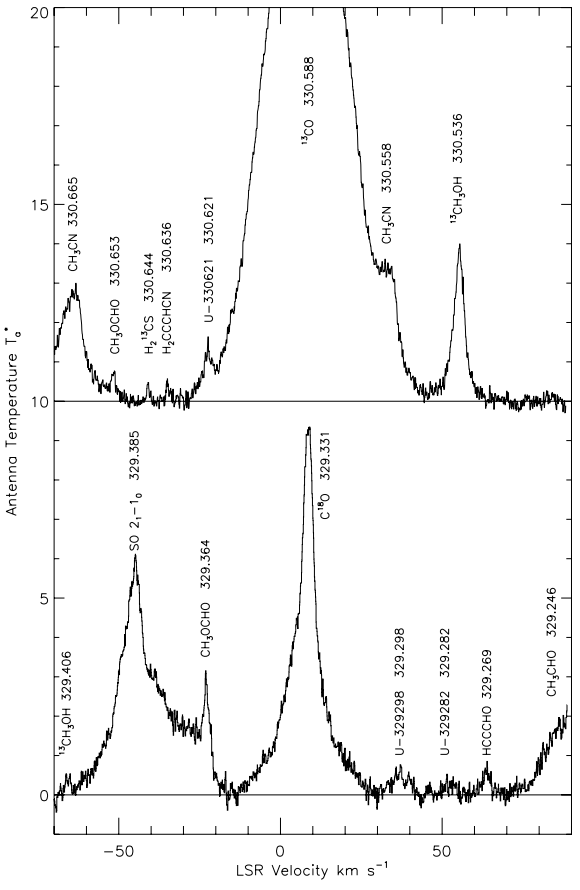

Figure 11. The spectra at the OMC 1 core position. The upper spectrum shows the complement of lines close to the ^{13}CO line, and the lower spectrum the lines close to C^{18}O.

Table 2. Lines detected in the ^{13}CO/C^{18}O passband.

Line	Transition	Frequency (GHz)	Lower energy
CH_3CHO	$6_{4,2}$–$6_{3,3}$	329.246	28
HC_3HO	$39_{2,38}$–$39_{0,39}$	329.269	239
U-329282		329.282	–
U-329298		329.299	–
C^{18}O	3–2	329.331	0
CH_3OCHO	$26_{7,19}$–$25_{7,18}$	329.364	0
SO	2_1–1_0	329.385	0
$^{13}CH_3OH$	$7_{5,2}$–$6_{2,5}$	329.406	326
$^{13}CH_3OH$	$7_{2,6}$–$6_{2,5}$	330.536	51
CH_3CN	18_9–17_9	330.558	0
^{13}CO	3–2	330.588	11
U330621		330.621	–
H_2C_3HCN	$46_{13,33}$–$47_{12,36}$	330.636	306
$H_2{}^{13}CS$	$10_{2,25}$–$27_{4,24}$	330.644	86
CH_3OCHO	$28_{3,25}$–$27_{4,24}$	330.653	161
CH_3CN	18_8–17_8	330.665	0

The OMC 1 region is known to contain several chemically and kinematically different gas components, in addition to the relatively cool and quiescent gas of the Orion complex: (a) a broad-line component in the OMC 1 core, associated with the molecular outflow/Orion bullets noted earlier, and centred in the vicinities of IRc2 (Genzel & Stutzki 1989), seen at velocities between 2.5 and 7.5 km s^{-1}; (b) the so-called compact ridge, a more quiescent, compact region which is distinguished by having high abundances of complex oxygen-bearing species, such as CH_3OH and CH_3OCHO, seen at velocities between 7 and 9 km s^{-1} and linewidths $\sim$10 km s^{-1}; (c) clumps of very dense ($\gtrsim 10^6$ cm^{-3}), warm ($\sim$200 K) material known as the hot core, seen at velocities between 2.5 and 7.5 km s^{-1}.

We list the line detections from the spectra in Table 2, some of which were strong enough and free of other line contamination to map, including SO, C_2H_5OH, CH_3OCHO and $^{13}CH_3OH$. The spatial distribution of these lines is shown in Fig. 12. All of the lines detected peak on the OMC 1 core, while none of the other lines in the two spectral windows was detected towards the Orion bar. The SO map shows a second peak, Orion-South, $\sim$1.5 arcmin south of the OMC 1 core (Kawamura et al. 2002) at 5^{h}35^{m}13^s.7, −5°24′09″ with a peak antenna temperature of $\sim$0.2 K and integrated intensity $\sim$1.5 K km s^{-1}.

4 ANALYSIS OF CLOUD PARAMETERS

CO is the most abundant molecular species after H_2, and these wide-field, high-resolution maps in the CO isotopologues ^{13}CO and C^{18}O are the best way to study the distribution, kinematics and physical characteristics of dense, star-forming molecular gas. In this section, we describe the general properties of Orion A using the emission characteristics of both isotopologues ^{13}CO and C^{18}O. In Section 4.1, we describe the large-scale kinematics of Orion A using the emission characteristics of ^{13}CO. We calculate the physical properties of the molecular gas in the following sections. The opacity of the $J = 3 \rightarrow 2$ transitions can be calculated from the line ratios, described in Section 4.2. The excitation temperature of the gas can then be calculated assuming conditions of local thermodynamic equilibrium (LTE), utilizing the opacity measurements, as described in Section 4.3. The opacity- and temperature-corrected mass, kinetic energy and gravitational potential energy of the bulk of

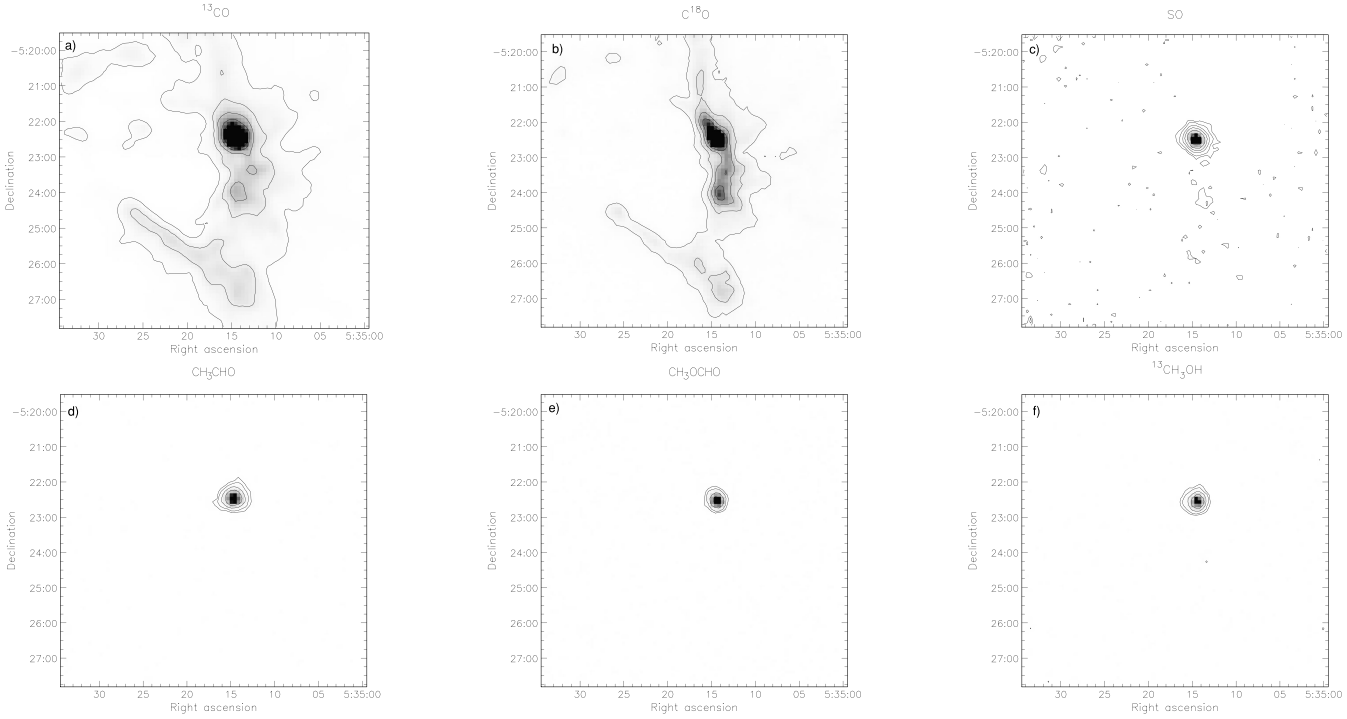

Figure 12. Maps of (a) ^{13}CO (first contour 50 K km s^{-1} and contour steps of 50 K km s^{-1} with peak intensity 607 K km s^{-1}), (b) C^{18}O (first contour 10 K km s^{-1} and contour steps of 10 K km s^{-1} with peak intensity 91 K km s^{-1}, (c) SO (contours at 1, 2, 5, 10, 20 and 40 K km s^{-1} with peak intensity 73 K km s^{-1}), (d) CH_3CHO (contours at 1, 2, 5 and 10 K km s^{-1} with peak intensity 27 K km s^{-1}), (e) CH_3OCHO (contours at 1, 2, 5 and 10 K km s^{-1} with peak intensity 13 K km s^{-1}) and (f) $^{13}CH_3OH$ (contours at 1, 2, 5 and 10 K km s^{-1} with peak intensity 22 K km s^{-1}) around the OMC 1 core and Orion bar regions.

the molecular gas can then be calculated using both isotopologues, along with the mass and energetics of high-velocity material using ^{13}CO, as described in Section 4.4.

4.1 Cloud kinematics

In Section 3, we described the velocity structure of numerous dense and/or energetic features detected in the CO $J = 3 \rightarrow 2$ isotopologues and associated with well-known Orion A regions. In this section, we look at the overall kinematics of the whole cloud, which we can then compare to the physical properties calculated in the following sections.

There is a clear red–blue velocity gradient running from north to south along Orion A. Fig. 13(a) shows the intensity-weighted velocity map in ^{13}CO, with C^{18}O contours marking the highest column density regions. The northern filament is at velocities 11–14 km s^{-1} and the southern filament is at velocities 5–8 km s^{-1}, with the highest column density region at the lowest velocity. The bulk of the ^{13}CO emission surrounding OMC 1 is at 9–10 km s^{-1}, but there are large regions embedded within this, with sizes up to several arcminutes, that are shifted in velocity to both the red and the blue. One of these is highlighted by a horizontal line in Fig. 13(a).

Fig. 14 shows an east–west PV slice of the region between OMC 1 and OMC 4 at a declination of $-5^\circ 31'$, where the velocity field moves through red–blue–red from east–west. The main filament at this declination lies at unusually high velocity ($\sim$13 km s^{-1}), whilst a bright, isolated and relatively compact cloud at the same position lies at much lower velocity of $\sim$6 km s^{-1}. This explains the unusual velocity field seen in Fig. 13. The isolated cloud is dominating the velocity calculation over a small area.

Fig. 13(b) shows the ^{13}CO intensity-weighted dispersion map. The central regions around OMC 1 contain gas with the highest velocity dispersions, if we exclude the region between OMC 1 and OMC 4, where the additional velocity component from the isolated cloud is confusing the dispersion calculations. The lowest dispersions are seen along the Orion bar. C^{18}O maximum intensity contours indicate regions of high column density. To the north and south, there are indications that the dispersion falls towards the highest column density regions, although all of the OMC regions contain protostellar sources.

4.2 Opacity

We can estimate the opacity of the CO isotopologue transitions based on the line-peak ratios of ^{13}CO/C^{18}O. The intensity ratio is related to the opacity through

$$R_{1318} = \frac{T_{\rm A}^*(^{13}{\rm CO})}{T_{\rm A}^*({\rm C}^{18}{\rm O})} = \frac{1 - \exp(-\tau_{13})}{1 - \exp(-\tau_{18})}. \quad (1)$$

We measure $T_{\rm A}^*(^{13}{\rm CO})$ and $T_{\rm A}^*({\rm C}^{18}{\rm O})$ at the velocity of peak intensity in the C^{18}O emission, and only include regions where C^{18}O is detected at levels $>5\sigma$. This method makes several assumptions about emission from the isotopologues (see e.g. Myers, Linke & Benson 1983; Ladd, Fuller & Deane 1998, for details): that the beam efficiency, filling factor and excitation temperature are the same for both isotopologues. As described in Section 2, there are sometimes multiple velocity components, particularly in the ^{13}CO emission, whose effect we mitigate using the ^{13}CO values at the velocity of the C^{18}O peak intensity, since this velocity best traces the underlying velocity of the cloud probed by emission from the isotopologues. We use the line peak, rather than the integrated intensity, to minimize the contribution of multiple velocity components to the ratio. We assume that the ratios of linewidths to the line-of-sight extent of the emitting gas are the same for the two isotopologues. Where both lines are optically thin, the ratio R_{1318} should tend to the abundance

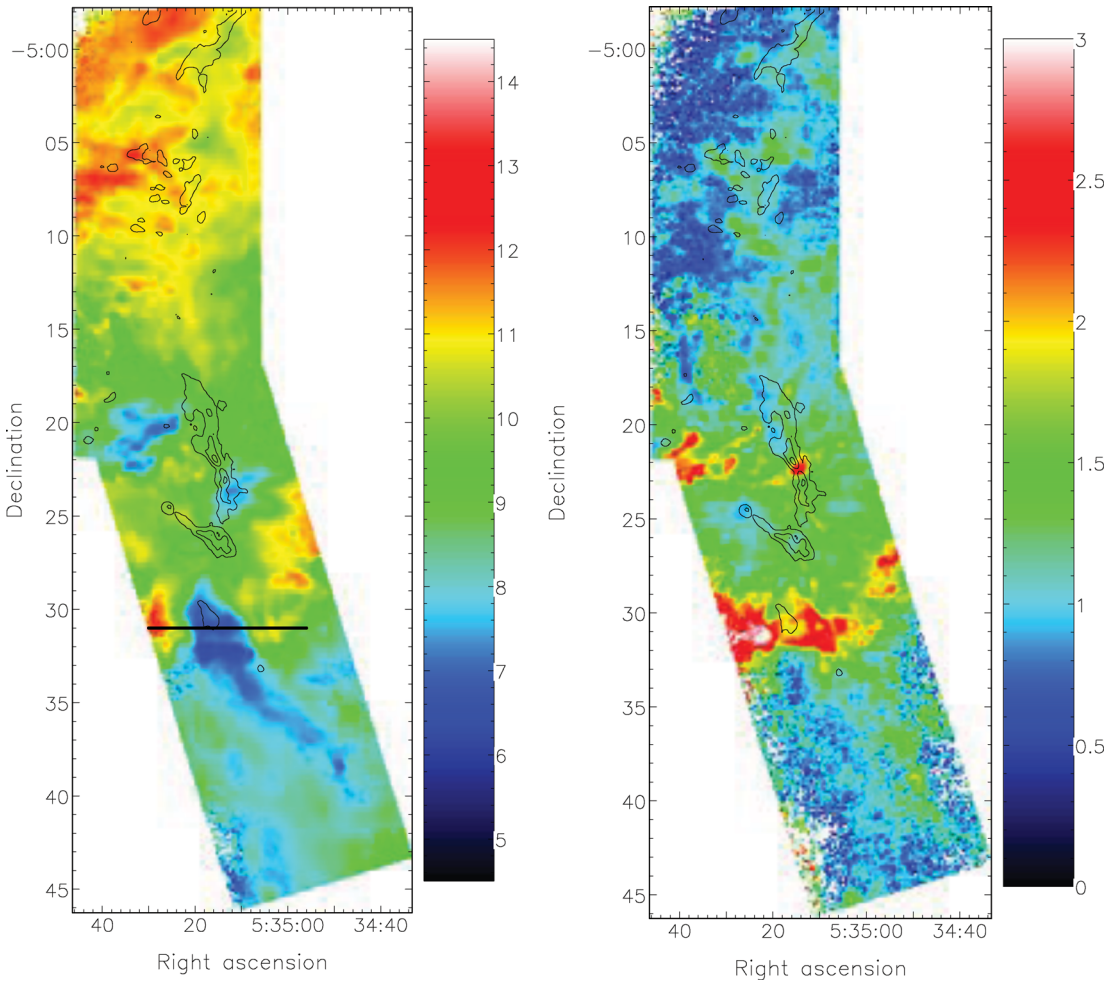

Figure 13. (a) ^{13}CO intensity weighted velocity map of Orion A, giving the velocity field in km s^{-1}. The black line marks the region between OMC 1 and OMC 4, and is the location of the PV slice shown in Fig. 14. (b) ^{13}CO intensity weighted dispersion map of Orion A, giving the velocity dispersion in km s^{-1}. C^{18}O contours mark the highest column density regions.

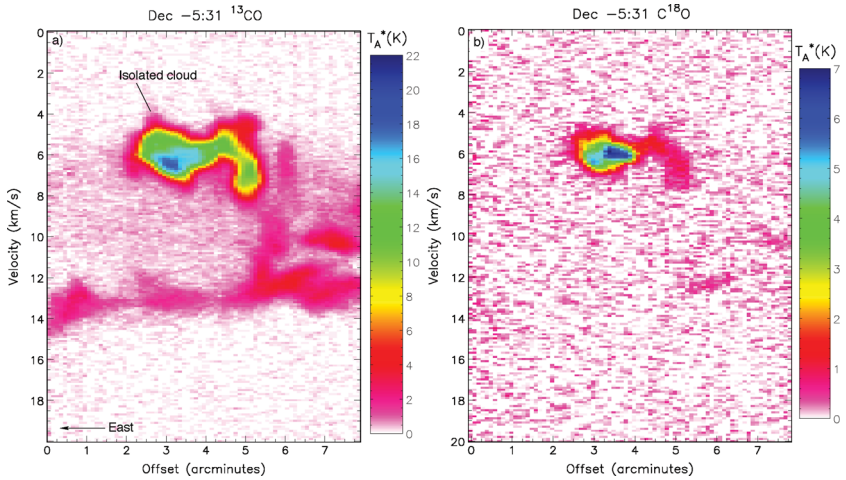

Figure 14. PV diagrams of the region between OMC 1 and OMC 4 (along the horizontal line shown in Fig. 13), showing (a) the ^{13}CO and (b) C^{18}O molecular tracers.

ratio previously determined to be $X[^{13}\mathrm{CO}/\mathrm{C}^{18}\mathrm{O}] = 8.4$ (Frerking, Langer & Wilson 1982; Wilson 1999).

The ^{13}CO/C^{18}O intensity ratio map is shown in Fig. 15. In regions of strong emission, the ^{13}CO/C^{18}O intensity ratio is generally low, ∼2. The ratio rises towards the edge of detected emission, with a median value of 4.7 ± 0.3 (uncertainties quoted are from the dispersion of tau values). In Fig. 15, we also show the distribution of intensity ratios for representative central, northern and southern regions. The regions to the north and south show similar peaks and distributions in the intensity ratio, with median values of

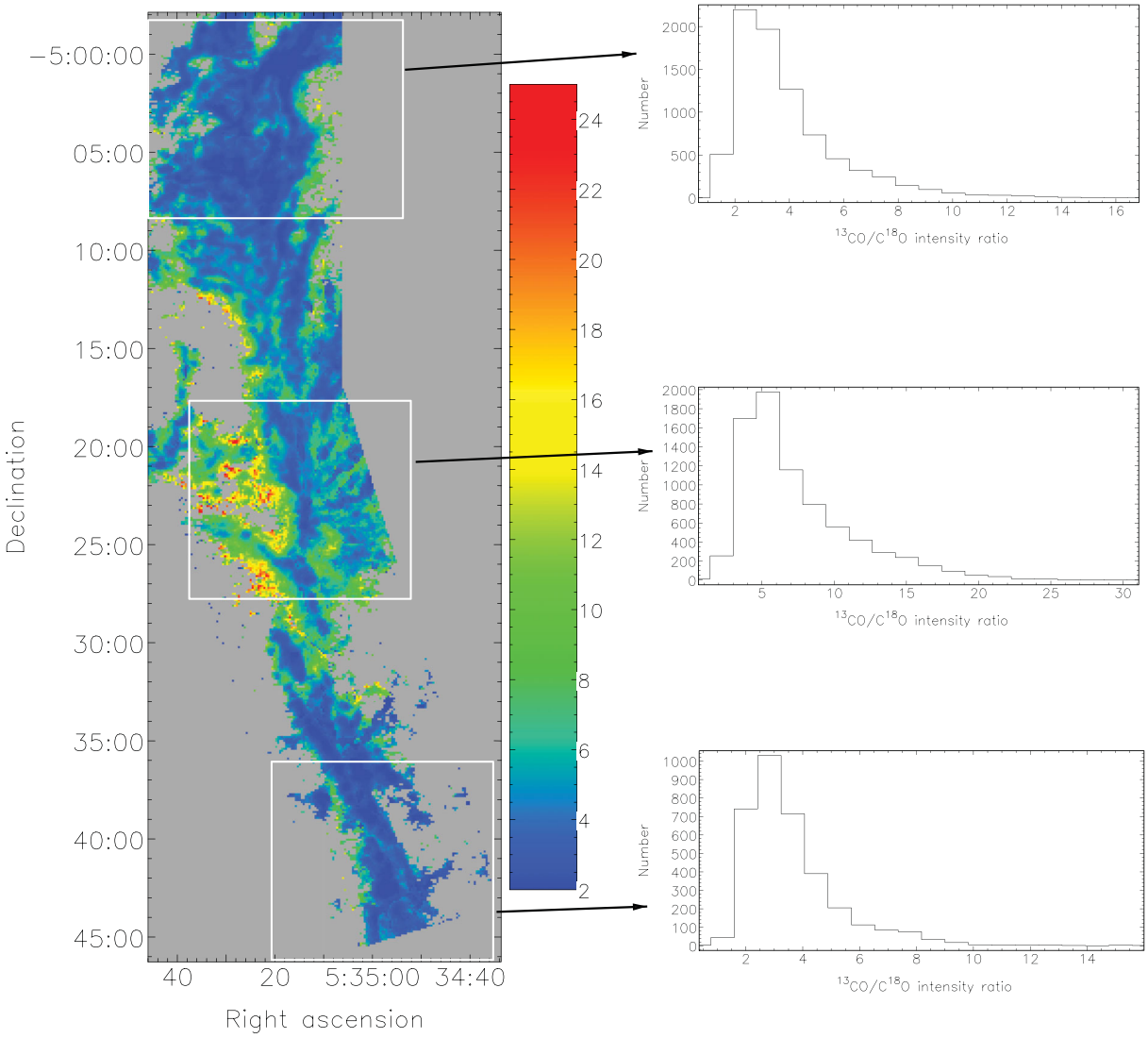

Figure 15. Map of ^{13}CO/C^{18}O intensity ratios for regions with C^{18}O detections $>5\sigma$. The plots show histograms of intensity ratio values for three different regions within the map.

3.5 ± 0.3 (north) and 3.4 ± 0.3 (south). The central region, near OMC 1, peaks at a higher value, with a median value of 6.4 ± 0.2. The distribution around OMC 1 also extends to higher values, >25.

At the edges of the ratio map, the emission arises in regions nearer to the cloud edges, and the increased ^{13}CO/C^{18}O ratio is consistent with selective photodissociation at the edge of the cloud, since self-shielding of ^{13}CO is more effective than for C^{18}O (Van Dishoeck & Black 1988; Beuther et al. 2000). In regions of strong C^{18}O emission, column densities are expected to be relatively high, which can protect C^{18}O from photodissociation (Zielinsky, Stutzki & Störzer 2000), leading to reduced ^{13}CO/C^{18}O ratios as we find. The region around OMC 1 has very strong emission from both isotopologues, and we measure much higher intensity ratios. This may be indicative of non-thermal excitation conditions in the region surrounding M43. High ^{13}CO/C^{18}O intensity ratios can also be explained if the CO emission arises in small clumps in a photodissociation region (Zielinsky et al. 2000). In this case, self-shielding of ^{13}CO is more effective than for C^{18}O.

Towards the edges of the northern and southern regions of the Orion A map, we find ratios between 7 and 10, which are consistent with the previously measured abundance ratio of ∼8.4, although our calculations are dependent upon the level at which the C^{18}O data are thresholded. We use the abundance ratio $X[^{13}\mathrm{CO/C^{18}O}] = 8.4$ to calculate the transition opacities. Median CO transition opacities are $\bar{\tau}_{18} = 0.24 \pm 0.17$ and $\bar{\tau}_{13} = 2.0 \pm 1.5$. The lower intensity ratio values in the north and south indicate higher opacities in these regions, assuming similar abundance ratios. Overall, the bulk of the C^{18}O emission is optically thin, while the bulk of the ^{13}CO emission is marginally optically thick.

4.3 Temperature

Assuming LTE, the excitation temperature (T_{ex}) of the gas can be calculated from the line-peak temperature (T_{max}) using the standard radiative transfer relation in an isothermal slab. Using the opacities calculated in Section 4.2, and assuming the emission fills the beam in the line core across the cloud, we have (e.g. Pineda, Caselli & Goodman 2008)

$$T_{\mathrm{mb}}(^{13}\mathrm{CO}\,3 \rightarrow 2) = \left[\frac{15.87\,\mathrm{K}}{\exp(15.87\,\mathrm{K}/T_{\mathrm{ex}}) - 1} - 0.045\right][1 - \exp(-\tau_{13})], \quad (2)$$

Table 3. Table of column densities, masses and energetics in Orion A. 1σ uncertainties are given in parentheses.

Isotopologue	L (pc)	$\sigma_{v,3D}$ (km s^{-1})	N(mol) ($\times10^{20}$) cm^{-2}	$N(H_2)$ ($\times10^{26}$ cm^{-2})	Mass ($M_\odot$)	E_{kin} ($\times10^{40}$ J)	$-W_{fil}$ ($\times10^{40}$ J)	M_H ($M_\odot$ pc^{-1})	M_H/M_{vir}	P ($M_\odot$ km s^{-1})
$C^{18}O$	5.76(0.01)	2.15(0.06)	1.30(0.06)	7.63(0.36)	2420(114)	1.11(0.05)	0.87(0.08)	420(20)	0.20(0.009)	
^{13}CO	5.76(0.01)	2.44(0.06)	18.9(0.05)	13.50(0.28)	4290(89)	2.53(0.05)	2.74(0.11)	745(15)	0.27(0.006)	
^{13}CO red					81(1.0)	1.7(0.02)				1180(16)
^{13}CO blue					74(1.0)	1.6(0.02)				1080(16)

$$T_{mb}(C^{18}O\,3\rightarrow2) = \left[\frac{15.81\,K}{\exp(15.81\,K/T_{ex})-1} - 0.045\right][1-\exp(-\tau_{18})]. \quad (3)$$

Under conditions of LTE, it is assumed that the excitation temperature is constant along the line of sight. Given that our observations of Orion A have several regions with multiple velocity components, such as is clearly seen in the PV diagrams of OMC 4 (Fig. 9), the calculated excitation temperature is that of the dominant $C^{18}O$ component along the line of sight, since this component will be the most significant contribution to the physical parameters of the cloud we are calculating. If the emission arises in clumps smaller than the telescope beam, then the actual temperatures will be higher than those derived here, since we assume a filling factor of unity. In addition, the excitation temperature is likely to underestimate the kinetic temperature of the gas, particularly across low volume density regions. In the higher volume density regions along most of the filament, the gas is heated primarily through collisions with the dust, and so the gas and dust are more likely to be thermally coupled.

The median excitation temperature we calculate from the ^{13}CO data set is 26 ± 4 K. For $C^{18}O$, we obtain 22 ± 6 K. Along the central parts of the OMC 1 filament, the excitation temperature increases to >70 K. The Orion bar also exhibits high excitation temperatures, >80 K.

Dust temperature measurements (T_{dust}) have been made from multiple wavelength observations of the dust towards the BN–KL region by Dicker et al. (2009), who calculate high temperatures in this region of $T_{dust} = 42 \pm 3$ K. We find higher temperatures for ^{13}CO with $T_{ex} = 58 \pm 4$ K, while for $C^{18}O$ $T_{ex} = 40 \pm 6$ K. The difference in excitation temperatures for the two isotopologues in these very dense regions may be due to different optical depths and hence different filling factors. We expect the more optically thin $C^{18}O$ transition to trace material deeper into the core and be more closely associated with the dust emission than the higher opacity ^{13}CO transition. In addition, this region is the one for which we find high $^{13}CO/C^{18}O$ intensity ratios, and the isotopic abundance we have assumed may not be correct. The Orion KL region has several components along the line of sight, with physical conditions ranging from 40 to 150 K, and densities of 10^5–10^7 cm^{-3} (Plume et al. 2012).

The dust component of the southern half of the filament has been studied at 850 μm using SCUBA (Johnstone & Bally 1999). The excitation temperatures we find for the molecular gas at the position of the 24 dust cores within our observed region agree with a median T_{dust}/T_{ex} ratio of 1.3 (^{13}CO, 1.4 for $C^{18}O$) to those found for the dust temperatures, with the CO excitation temperatures lower than the dust temperatures.

4.4 Mass and energetics

The CO $J = 3 \rightarrow 2$ isotopologue transitions are excited in warm, dense gas that is closely associated with active star formation activity. In this section, we assess the physical properties of the molecular gas in relation to the sites of active star formation. We calculate the mass in the large-scale cloud from $C^{18}O$ column densities, assuming LTE conditions prevail. Detailed multitransition observations of $C^{18}O$ towards Orion KL (Plume et al. 2012) suggest that LTE is a reasonable assumption in the Orion A region. We use the excitation temperatures and opacities previously calculated (Sections 4.2 and 4.3). The total gas mass is calculated from total column densities (Garden et al. 1991; Buckle et al. 2010) so that

$$M_{gas} = 1.13\times10^{-4}\,\mu_{H_2}\,m_H\,d^2\,\Delta\alpha\,\Delta\beta\,\frac{1}{X}\sum N(CO)\quad (M_\odot), \quad (4)$$

where the sum is carried out across all pixels with $C^{18}O$ emission detected at $>5\sigma$. $\Delta\alpha\Delta\beta$ is the pixel area (36 arcsec^2), d is the distance in pc and X is the isotopic abundance ratio of the CO isotopologues relative to H_2. We adopt a mean molecular weight per H_2 molecule of $\mu_{H_2} = 2.72$ to include helium, and $X[^{13}CO] = 1.4\times10^{-6}$ and $X[C^{18}O] = 1.7\times10^{-7}$ (Frerking et al. 1982; Wilson 1999). We adopt a distance of 415 pc to Orion A. The results are shown in Table 3.

We find total H_2 column density of 7.63×10^{26} cm^{-2} (13.5×10^{26} cm^{-2}) for $C^{18}O(^{13}CO)$. We find a total mass, using $C^{18}O$ emission, of 2420 $M_\odot$ in Orion A, with the filament extending across 5.76 pc. For ^{13}CO, we find a total mass 1.77 times greater. The difference in masses calculated from the two isotopologues may be due to differences in structure within the beam. Beuther et al. (2000) found that ^{13}CO beam filling factors could be double of those of $C^{18}O$ in the highly clumped Cepheus B cloud, using multiwavelength CO isotopologue observations. The mass of the dust contained within the Orion A cores (Di Francesco et al. 2008, The SCUBA Legacy core catalogue) is much lower, at 1208 $M_\odot$.

Bally et al. (1987) measured 5000 $M_\odot$ from ^{13}CO observations, which extended over a much larger region covering 13 pc. A comparison with the results presented here suggests that most of the mass in the extended filament is concentrated in the active star-forming region covered by our data. The regions containing the most mass are the Orion nebula, as also found by Bally et al. (1987), and the Orion bar. These are also the regions that have the highest excitation temperatures.

In order to characterize the equilibrium state of the Orion A cloud, we have used a virial analysis of the filamentary structure within which the OMC regions are embedded. The gravitational potential energy, W_{grav}, of the cloud can be calculated using a cylindrical model (Fiege & Pudritz 2000). These authors show that a filamentary cloud model with a helical magnetic field matches observed density profiles, and apply the virial theorem to these structures. The resulting virial relations can be used to test the Larson laws in filamentary cloud models in a similar manner to those of spherical models, with resulting values of $0.11 \leq M/M_{vir} \leq 0.43$.

The total kinetic energy, E_{kin}, can be calculated by estimating the three-dimensional velocity dispersion, $\sigma^2_{v,3D}$ (given in Table 3), from the one-dimensional velocity dispersion, $\sigma_{^{13}CO}$ or $\sigma_{C^{18}O}$. We

use the average intensity-weighted velocity dispersion, normalized by the integrated intensity, taken over the regions detected at $>5\sigma$ for each isotopologue to calculate this parameter. We also use $\sigma^2_{\rm v,3D}$ to calculate the virial mass per unit length for the cylindrical model, $M_{\rm vir}$. We use the following calculations:

$$M_{\rm vir} = \frac{2\left\langle\sigma^2_{\rm v,3D}\right\rangle}{G}, \tag{5}$$

$$W_{\rm grav} = -\frac{GM^2_{\rm gas}}{L}, \tag{6}$$

$$E_{\rm kin} = \frac{1}{2}M_{\rm gas}v^2, \tag{7}$$

$$v^2 = \left\langle\sigma^2_{\rm v,3D}\right\rangle = 3\left[\left\langle\sigma^2_{\rm CO}\right\rangle + \frac{kT}{m_{\rm H}}\left(\frac{1}{\mu} - \frac{1}{m_{\rm CO}}\right)\right], \tag{8}$$

where G is the gravitational constant, k is Boltzmann's constant, T is the kinetic temperature of the gas, which we have taken to be equal to the median excitation temperature of the isotopologues, $m_{\rm CO}$ is the atomic mass of ^{13}CO, or C^{18}O, and $\mu = 2.33$ is the mean molecular weight per particle. The median thermal contribution to the velocity dispersion is 0.2 km s^{-1} for both isotopologues. L is the length of the cylinder measured from the total length of detected emission above the 5σ level along the Orion A filament (given in Table 3). The LTE column densities, masses, kinetic and gravitational potential energies of Orion A are listed in Table 3.

The $M_{\rm H}/M_{\rm vir}$ results calculated using data from both isotopologues are similar to those found for Orion A by Fiege & Pudritz (2000, $M_{\rm H} = 355$, $M_{\rm H}/M_{\rm vir} = 0.38$) using the data of Bally et al. (1987). Values of $M_{\rm H}/M_{\rm vir} \ll 1$ are consistent with a filamentary structure threaded by helical magnetic fields (Fiege & Pudritz 2000). A previous study on a low-mass star-forming region (Perseus, Hatchell et al. 2005) using dust continuum data found $M_{\rm H}/M_{\rm vir} \sim 1$, and so no requirement for magnetic support.

The critical factor in determining collapse in the filament is the mass per unit length, $M_{\rm H}$, with $M_{\rm H\,crit} = 2c_{\rm s}^2/G \sim 37\,{\rm M}_\odot\,{\rm pc}^{-1}$ for an unmagnetized cloud, where $c_{\rm s} \sim 0.3\,{\rm km\,s}^{-1}$ is the isothermal sound speed for $T \sim 26$ K, as in Orion A. The presence of magnetic fields can increase the critical value by a factor of 2 (Fiege & Pudritz 2000). In a magnetized cloud, $M_{\rm H\,crit}$ is the equivalent of $M_{\rm vir}$ for an unmagnetized cloud.

André et al. (2010) found a column density threshold for star formation of $N({\rm H_2}) = 10^{22}\,{\rm cm}^2$, initially identified by locating protostars in column density maps (Onishi et al. 1998), corresponds to a critical mass per unit length for fragmentation in filaments of $15\,{\rm M}_\odot\,{\rm pc}^{-1}$ (assuming a temperature of 10 K; Ostriker 1964). In Orion, the mass per unit length threshold is higher, but is still exceeded along the filament, with $M_{\rm H}/M_{\rm H\,crit} = 10$–$20$. In a magnetized cloud, $M_{\rm H\,crit}$ can be higher, but even so $M_{\rm H}/M_{\rm H\,crit} \gg 1$. This is reflected in a high level of star formation throughout this region (Davis et al. 2009). Although not all the cloud cores are involved in star formation at the current time (see Section 5), the high $M_{\rm H}/M_{\rm H\,crit}$ ratio along the filament suggests that these regions will go on to form stars. The total mass of dust cores (Di Francesco et al. 2008, The SCUBA Legacy core catalogue) also suggests that Orion A is well above the threshold for collapse, with $M_{\rm H} = 209\,{\rm M}_\odot\,{\rm pc}^{-1}$.

For the energetics in the redshifted and blueshifted gas, we use ^{13}CO data cubes that are redshifted and blueshifted relative to the velocity of the optically thin C^{18}O gas. This enables us to more accurately calculate the energy traced only in the high-velocity line wings of ^{13}CO across the whole cloud, taking into account the velocity shift between the northern and southern components. Using the extent of the redshifted and blueshifted gas, we base these calculations on a velocity region of 12 km s^{-1} across the line wing, specifying the line core to be the central 5 km s^{-1} across the C^{18}O line and using $\pm$ 14.5 km s^{-1} as the maximum velocity for the redshifted and blueshifted gas. The excitation temperature of emission from gas entrained in the outflows is likely to be higher than that of the cores, and so we adopt a temperature of 50 K for the mass calculations (e.g. Hatchell, Fuller & Ladd 1999; Davis et al. 2010).

The redshifted and blueshifted emission of ^{13}CO contain very similar masses and energetics, with a total of $\sim 80\,{\rm M}_\odot$ in each of the red and blue outflow components. Although ^{13}CO does not trace the highest velocity flows as well as ^{12}CO, we find a total of $3.3\times\ 10^{40}$ J of kinetic energy, with OMC 1 having the most significant contribution in mass, kinetic energy and momentum. The large amount of star formation activity results in $\sim$3 per cent of the molecular cloud gas mass being swept up and entrained in the outflows.

5 C^{18}O PROPERTIES OF THE SCUBA LEGACY CATALOGUE CORES

Continuum submillimetre emission is often used to identify star-forming and potentially star-forming cores within molecular clouds. In order to understand the physical conditions of these objects, the velocity information found in spectral line observations is vital. We have used our observations of the C^{18}O optically thin tracer to look at the variation in the physical conditions of the cores and to investigate the size scales on which the Larson relations, derived for entire molecular clouds and giant molecular clouds (GMCs), break down.

To identify the dense cores, we use the SCUBA Legacy Catalogue (SLC; Di Francesco et al. 2008), which is based on a structural analysis of the SCUBA continuum images. These analysis techniques are currently more robust when carried out on two-dimensional imaging data sets, rather than three-dimensional spectral imaging data sets. The GBS is currently working to develop algorithms that can be used on spectral imaging data sets, and applied to all of the regions observed by the survey.

The SLC cores were identified using the CLUMPFIND algorithm (Williams, Blitz & Stark 1995). Each of the cores is characterized by Sadavoy et al. (2010a) as starless or protostellar based on *Spitzer* IR colours and proximity of IR sources to SLC peak positions. Outlines of the SLC cores are shown in Fig. 16, overlaid on the integrated C^{18}O emission. Cores identified by Sadavoy et al. (2010a) as protostellar are shown as squares, and those identified as starless are shown as crosses. Since Sadavoy et al. (2010a) classified cores according to detections of protostellar-like IR sources, the reliability of these classifications is dependent on the quantitative characteristics and detection of IR emission towards each core. In very crowded regions like OMC 1, IR emission towards a core can be obscured or contaminated – i.e. from IR emission of nearby more evolved YSOs, for example, emission from outflow shocks – altering the IR properties. Thus, the massive OMC 1 cores may contain undetected protostars (see Sadavoy, Di Francesco & Johnstone 2010b, for further discussion on the ambiguous nature of most of the OMC 1 cores).

The terms *clump* and *core* are broadly used for, respectively, substructures within a cloud and individual condensations that could form stars (see e.g. Williams, Blitz & McKee 2000, for further discussion of structure categorization and nomenclature); the

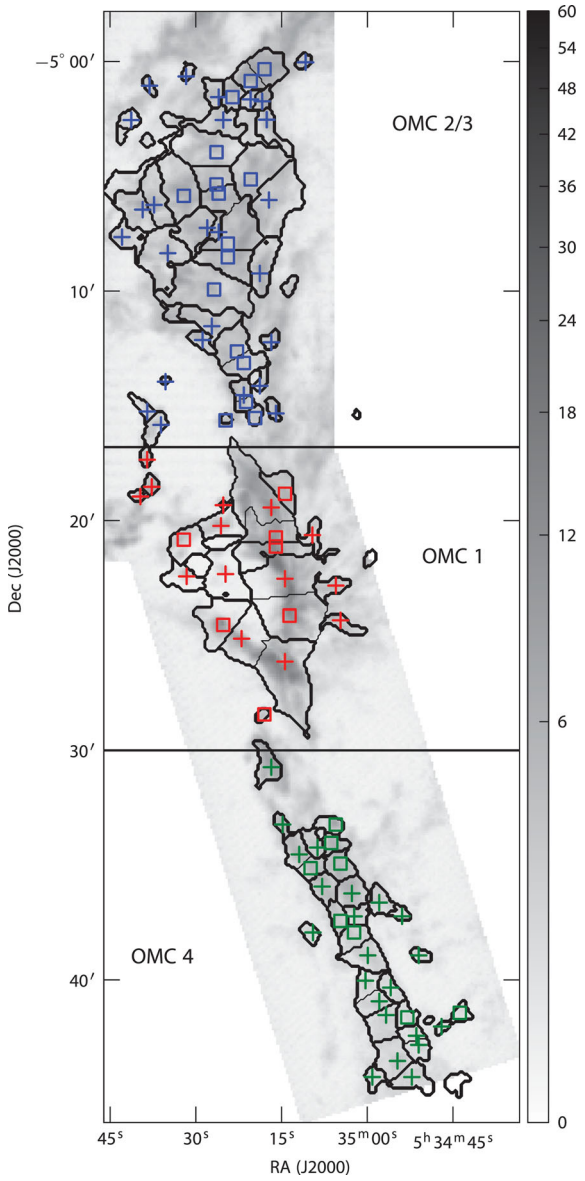

Figure 16. Outlines of the SLC cores overlaid on the $C^{18}O$ integrated intensity map. Cores are marked as protostellar (squares) or starless (crosses). Horizontal lines mark the declination cut we have used to separate OMC 2/3, OMC 1 and OMC 4.

classification of objects is dependent on the resolution of the observations. Some of the SLC cores, particularly towards the central OMC 1 region, are massive (∼several × 10^2 $M_\odot$) and spatially extensive, and likely to contain within them multiple starless and protostellar cores. With this caveat, we adopt the classifications of Sadavoy et al. (2010a) and use the position and size of the continuum cores, as shown in Fig. 16, to extract the $C^{18}O$ parameters used in the following analysis. We have separated the core populations into the central, northern and southern regions – OMC 1, OMC 2/3 and OMC 4, respectively; Fig. 16 shows the declination cuts used to divide the map into these regions.

One method of measuring the physical state of molecular gas is to examine the variation of turbulent support through the variation of velocity dispersion. We use the FWHM, Δv, of the individual $C^{18}O$ spectrum at the SLC peak to obtain the one-dimensional velocity dispersion, $\sigma_{CO} = \Delta v/\sqrt{8\ln(2)}$, after resmoothing the $C^{18}O$ data with an additional Gaussian beam to match the 22.9 arcsec effective convolved beam size of the reduced SLC data. The FWHM was estimated from the number of channels with an intensity greater than 50 per cent of the peak value for that spectrum. Fig. 17(a) shows histograms of velocity dispersion for the cores within the three spatial regions. OMC 1 has the largest and most massive cores, with larger linewidths towards the position of OMC 1 itself, with the distribution peaking at $\sigma = 0.66\,\mathrm{km\,s^{-1}}$. The cores in OMC 2/3 (peak $\sigma = 0.47\,\mathrm{km\,s^{-1}}$) and OMC 4 (peak $\sigma = 0.47\,\mathrm{km\,s^{-1}}$) have smaller linewidths, as is shown generally for these regions from the intensity-weighted dispersions map in Fig. 13. OMC 1 shows one outlier with a very broad velocity dispersion, which is the central core containing the BN–KL region.

The average values of σ_{CO} for each population are shown in Table 4. This shows both higher values and higher variation in the OMC 1 region compared to OMC 2/3 and OMC 4, but little variation between the starless and protostellar populations.

We can use the excitation temperature to investigate the physical state of the gas in the SLC cores. This was calculated based on the peak ^{13}CO emission (equation 2) within each SLC core boundary. The median and mean excitation temperature for each core classification is shown in Table 4, and the distribution of the cores is shown in Fig. 17(b). The starless and protostellar populations both have a large distribution of values in their excitation temperatures, and mean values of 26 and 30 K, respectively. While the starless cores peak at a lower temperature than the protostellar cores, both populations cover roughly the same range of temperatures (see Fig. 17b and Table 4).

The populations of cores based on their position in the filament give mean excitation temperatures ranging from 20 to 38 K and the OMC 2/3 and OMC 4 populations have a lower distribution of values (with standard deviations of 4.7 and 6.3). This suggests that the dominant effect governing the temperature of the core is its position in the filament, rather than its classification as starless or protostellar. Jijina, Myers & Adams (1999) found, using ammonia observations of dense cores in a range of star-forming regions, that cluster associations have much larger linewidths, kinetic temperatures and core sizes than more isolated environments. In Orion A, OMC 1 has a larger excitation temperatures and linewidths (Fig. 17c), although the linewidths are much larger than thermal for all of the regions.

5.1 The masses and fluxes of the SLC cores

Using the continuum and molecular line data, we have two independent methods of deriving the mass contained within the spatial extent of each SLC core. As shown in Fig. 16, the SLC core outlines and the $C^{18}O$ integrated intensity map appear visually to trace similar structures, and so, assuming a constant gas-to-dust ratio across Orion A, we might expect the masses derived from the SCUBA data and from the $C^{18}O$ data to be equal. Both of these mass derivations involve different assumptions and sources of uncertainty, which we can investigate through variations in the ratio of the two calculated masses for each core.

For each SLC core, we calculate the $C^{18}O$ total flux within the boundary of the SLC core and over the velocity range 1.0–15.0 $\mathrm{km\,s^{-1}}$, apart from the core containing OMC 1, which used −20.0 to 31.0 $\mathrm{km\,s^{-1}}$. These velocity ranges covered the full range of detected emission. This total flux gives the $C^{18}O$ mass (M_{C18O}) using equation (4). The SLC 850 μm flux masses (M_{850}) are calculated as

$$M_{850} = \frac{S_{850} d^2}{\kappa_{850} B_\nu (T_{\mathrm{dust}})} = 1.6\, S_{850}\ (\mathrm{M}_\odot), \qquad (9)$$

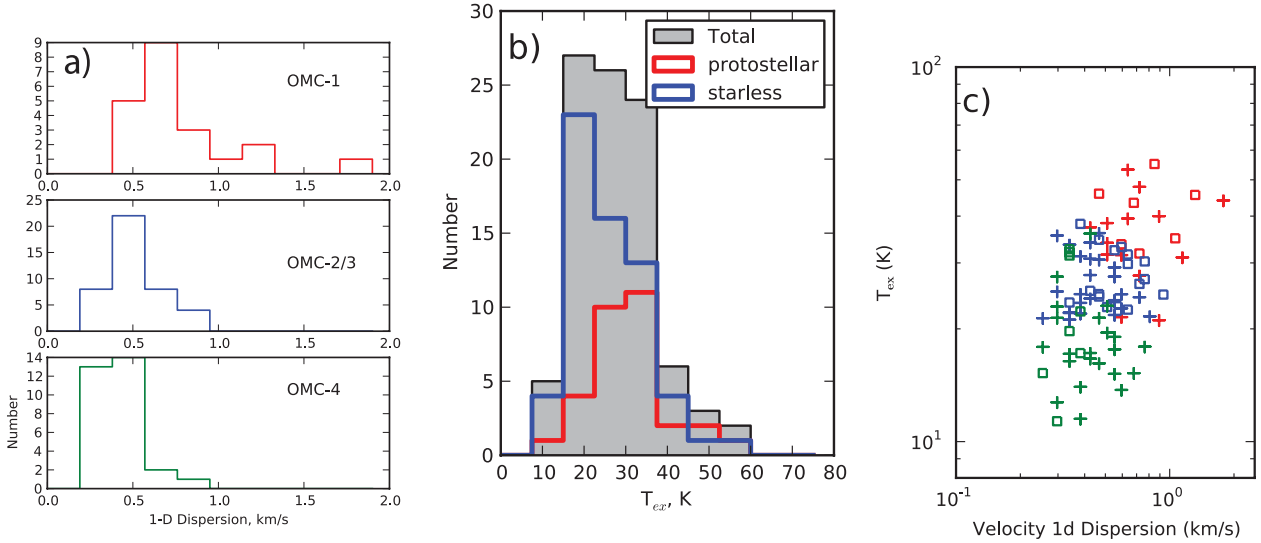

Figure 17. (a) Histograms of the one-dimensional velocity dispersion for the SLC cores in OMC 1, OMC 2/3 and OMC 4. (b) Histograms of the ^{13}CO calculated excitation temperature for the SLC cores by classification as starless, protostellar or both. (c) The relationship between T_{ex} and the C^{18}O velocity dispersion at the SLC peak. Coloured points are as (a), with square and crosses marking protostellar and starless cores, respectively.

Table 4. The median, mean and the standard deviation of the sample for the one-dimensional velocity dispersions at the 850 μm peak of each core, and the ^{13}CO calculated gas excitation temperature for each core. The values are given for the three spatial populations, as well as the protostellar and starless populations.

	σ_{CO} (km s^{-1})			T_{ex} (K)		
	Med.	Mean	Std.	Med.	Mean	Std.
Protostellar	0.51	0.57	0.239	30.3	29.8	9.22
Starless	0.467	0.52	0.236	23.5	25.7	8.76
OMC 1	0.679	0.775	0.32	37.3	37.6	8.97
OMC 2/3	0.467	0.504	0.154	25.0	27.1	4.71
OMC 4	0.382	0.416	0.124	17.8	19.7	6.3

where S_{850} is the 850 μm flux (Jy), T_{dust} is the temperature of the dust, $B_\nu(T)$ is the Planck function for temperature T and κ_{850} is the dust opacity, here taken to be 0.01 cm^2 g^{-1} (gas+dust) following Nutter & Ward-Thompson (2007) and André, Ward-Thompson & Motte (1996). This dust opacity originates in the modelling study of Stognienko, Henning & Ossenkopf (1995) and is the recommendation of Henning, Michel & Stognienko (1995) for dense gas $n_{H_2} \sim 10^5$. Recent measurements of the dust opacity in the isolated dense core B335 give a range of $\kappa_{850} = (1.18\text{–}1.77)^{+0.36}_{-0.24}$ cm^2 g^{-1} (per mass of dust; Shirley et al. 2011). If the standard gas-to-dust ratio of 100:1 by mass is assumed, then the opacity used here lies at the low end of this range ($0.01 \times 100 = 1.0$). However, the gas-to-dust emission ratio varies between regions and is particularly low in Orion, by around a factor of 3 or ∼33:1 (Goldsmith et al. 1997). Whether this is due to a change in grain properties leading to more effective dust emission or a difference in the ratio of gas and dust masses, it suggests that an opacity of 0.04–0.06 cm^2 g^{-1} would be more appropriate in this region and masses from dust emission (which are proportional to $1/\kappa_{850}$) could be overestimated by up to a factor of 6. The dust temperature is taken to be equal to the gas kinetic temperature T_{kin}, as appropriate for a dense environment, assuming that local thermal equilibrium applies, so $T_{kin} = T_{ex}$, where T_{ex} is the ^{13}CO excitation temperature (Section 5).

The mass ratio has a best-fitting power-law relation of

$$M_{C18O} \propto M_{850}^{1.38\pm0.17} \text{ protostellar cores,} \quad (10)$$

$$M_{C18O} \propto M_{850}^{1.18\pm0.11} \text{ starless cores.} \quad (11)$$

Fig. 18(a) plots the M_{C18O} against M_{850} for each core. Crosses and boxes denote starless and protostellar cores, respectively, and the red, blue and green colour coding denotes cores in OMC 1, OMC 2/3 and OMC 4, respectively.

To examine whether monotonic correlations exist between the two mass estimates, the Spearman correlation coefficient (Conover 1998) ρ is calculated for each population (starless or protostellar). We consider $|\rho| < 0.5$ an extremely weak correlation, $0.5 < |\rho| < 0.75$ a medium correlation and $0.75 < |\rho|$ a strong correlation. We give the P-value (P) of these results, with P-values less than the threshold $P = 0.05$ indicating a statistically significant result.

There is a strong correlation between M_{C18O} and M_{850}, with $\rho = 0.89$, $P < 0.0001$ for the protostellar cores and $\rho = 0.85$, $P < 0.0001$ for the starless cores. The correlation of the two independent (apart from the temperature assumption) mass calculations suggests we are measuring the true mass within the cores. Our calculations suggest there are systematic variations in our two measurements.

The mean ratio of masses $M_{850}/M_{C18O} = 0.6$, which may indicate that a warm envelope that surrounds the inner dense core is contributing significantly to the observed molecular line emission (Lee et al. 2003). Other effects, such as opacity or depletion, would increase the M_{850}/M_{C18O} ratio, which we do not see for the majority of cores.

Only a small number of the massive cores have $M_{850}/M_{C18O} > 1$. This could be due to variations of the dust opacity between the low-mass and the high-mass cores, or due to variations in the gas-to-dust ratio. The higher mass cores have, in general, a higher M_{850}/M_{C18O} ratio. Increased gas opacity and depletion of molecular gas could lead to increased 850 μm masses in proportion to the C^{18}O masses, although it is not clear why the higher mass cores would be more significantly affected. The effect of ^{12}CO $J = 3 \rightarrow 2$ contamination of the 850 μm fluxes in Orion was examined by Johnstone, Boonman & van Dishoeck (2003), who found that the contamination was

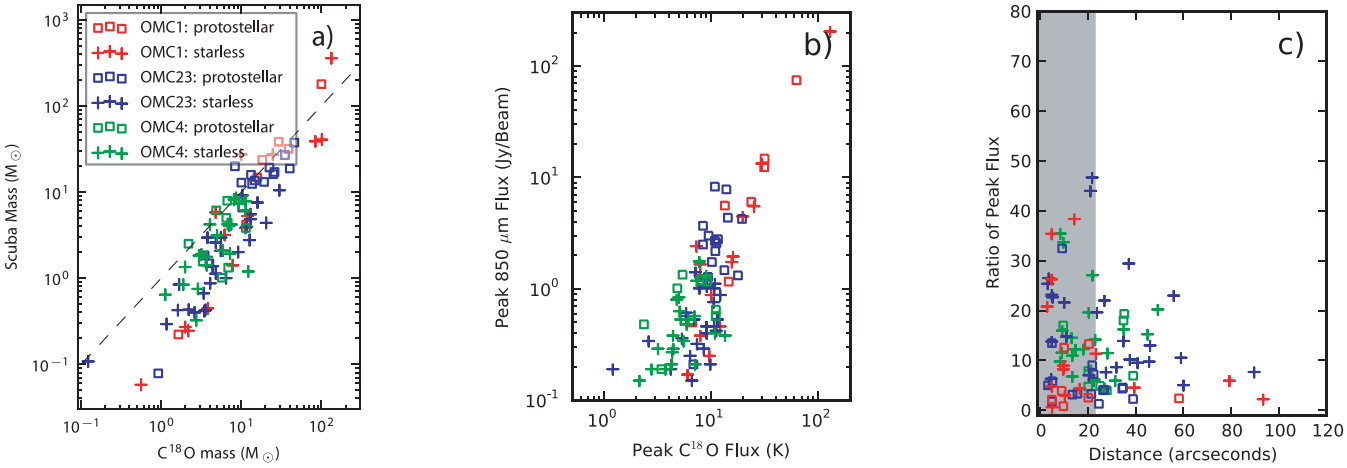

Figure 18. (a) The relationship between M_{850} and M_{C18O}. The dashed line indicates where equal masses would fall. For all three figures, crosses and boxes denote starless and protostellar cores, respectively, and the red, blue and green colour coding denotes cores in OMC 1, OMC 2/3 and OMC 4 respectively, as listed in the key. (b) The correlation between the SCUBA 850 μm peak flux and $C^{18}O$ integrated intensity from a single spectrum at the same position (in K km s^{-1}). (c) Ratio of $C^{18}O$ integrated intensity to SLC 850 μm flux at the position of the SLC 850 μm peak plotted against the spatial offset between the $C^{18}O$ and 850 μm peak positions. The shaded area indicates the resolution limit of the data set.

less than 10 per cent towards protostellar sources, although considerably higher towards positions in shock fronts within a PDR. If CO contamination were significantly affecting our results, we would expect the true core dust mass to be lower, especially towards the highly energetic, massive sources. CO contamination is therefore not the reason for elevated dust masses in a few of the massive cores.

There are large uncertainties in the estimates of both masses, including those from our estimation of the temperature – if the lower mass cores that are far from OMC 1 have systematically lower true temperatures than our estimated temperature, their true masses will be higher. Similarly, if the higher mass cores towards OMC 1 have a higher true temperature, their calculated masses will be lower.

Fig. 18(b) shows the relationship between the peak SLC 850 μm flux (in Jy beam^{-1}) and $C^{18}O$ peak intensity (in K) at the same position within each core. There is a medium monotonic correlation between the values $\rho = 0.69$, $P < 0.0001$ for the protostellar and $\rho = 0.57$, $P < 0.0001$ for the starless cores. The flux ratio varies between the OMC regions. The OMC 4 sources are all clustered towards the lower mass end of the graph. The OMC 2/3 sources are interspersed with the OMC 4 sources, but there is a population of OMC 2/3 protostellar cores which appear to have a higher SLC 850 μm peak flux without a significantly higher $C^{18}O$ peak flux.

The $C^{18}O$ and the 850 μm emission do not always peak in the same place, suggesting that the dust and the $C^{18}O$ emission do not trace the same physical structures in the inner cores. The poor correlation between the two measures at the peak may be caused by the large spatial extent of these cores, which may contain significant substructure and multiple embedded sources.

We have examined the spatial offset, in arcseconds, between the peak of the $C^{18}O$ emission and the peak of the SLC 850 μm emission within each core. This is shown in Fig. 18(c), plotted against the ratio of $C^{18}O$ integrated intensity at the SLC peak position and SLC 850 μm peak flux. There are cores from the centre of OMC 1 that show both large separations and ratios near unity, suggesting these cores have very different $C^{18}O$ and 850 μm distributions. However, many of the cores in OMC 1 are clustered below the resolution limit (indicated by the shaded region in Fig. 18c), and we do not detect these as having an offset $C^{18}O$ peak. There are many cores with large offsets and small ratios of peak flux, suggesting that $C^{18}O$ emission may be suppressed at the position of the SLC peak in these cores.

We have shown that $C^{18}O$ $J = 3 \rightarrow 2$ and 850 μm emission are tracing roughly the same structures on large spatial scales in Orion A. Fig. 18(a) shows this trend in the strong correlation between the two measurements. On smaller scales, there is substantial variation between the structures traced. This smaller scale variation is seen in Figs 18(b) and (c). High-resolution observations of the detailed physical processes interior to the cores are needed to disentangle the effects contributing to the variation in the structures traced by these two measurements.

5.2 The Larson relations

The Larson relations (Larson 1981) were found by examining the properties of entire molecular clouds. The linewidth–size relation ($\sigma \propto R^a$) suggests that the turbulent velocity dispersion of a structure is related via a power law to the size of the structure. Larson (1981) found $a \sim 0.5$. Heyer & Brunt (2004) looked at extending this to substructures within a cloud through the use of structure functions, finding that these also followed this relation. The Larson relations originate in the turbulent properties of molecular clouds on large scales; at smaller size scales, the relationships break down due to the increasing dominance of gravity and the transition to 'coherent' (subsonic) linewidths (Goodman et al. 1998). By examining subcloud-scale objects, we can constrain where this transition occurs.

We have used the one-dimensional velocity dispersion (σ_{CO}) and the effective radius of the SLC core ($R_{eff} = \sqrt{\text{area}/\pi}$) to examine the linewidth–size relation in Orion A, shown in Fig. 19(a). There is no good evidence for a correlation between σ and R_{eff} for the starless cores in Orion A, with $\rho = 0.25$, $P = 0.05$. For the protostellar cores, we calculate a medium monotonic correlation with $\rho = 0.62$, $P = 0.0002$ for the linewidth–size relation. For neither sample is the correlation strong enough to attempt a power-law fit. This lack of a clear correlation was also found by Curtis (2008). However, we are probing a limited range of sizes, with an effective radius between

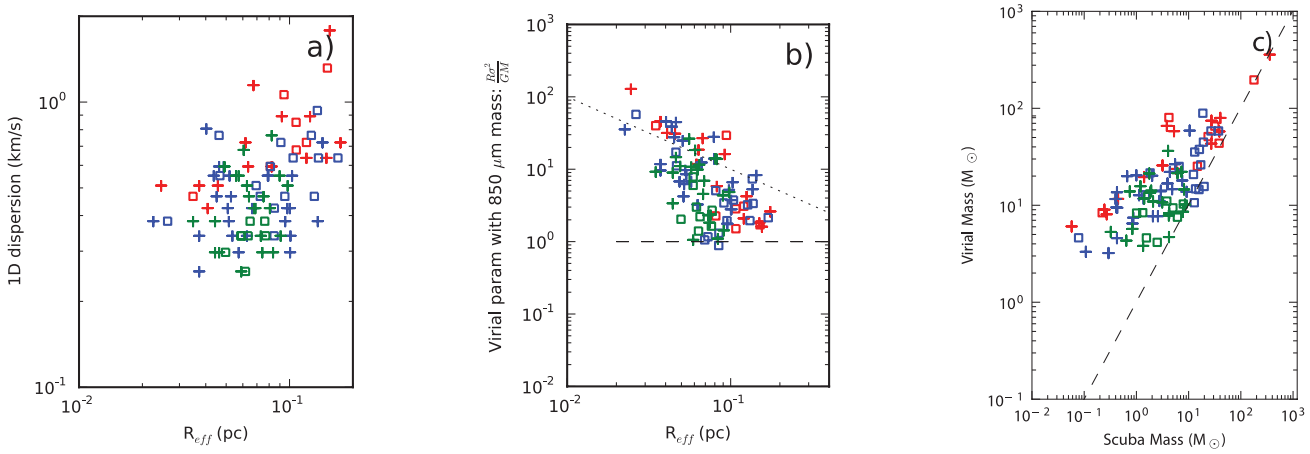

Figure 19. (a) Linewidth–size relation. The effective radius of the core plotted against the $C^{18}O$ velocity dispersion at the SLC peak. (b) The relation between the effective radius of the core and the virial parameter. The dotted line shows R against $1/R$. (c) The relation between the virial mass and the SLC 850 μm mass. The dashed line indicates where cores in virial equilibrium would be expected to lie. Cores in free fall would lie on the right-hand side; pressure-confined cores would lie to the left. For all figures, the key is as Fig. 18(a).

0.02 and 0.2 pc. Combined with the intrinsic scatter in this relation, this may prevent us detecting any relation here.

The second Larson relation suggests that the clouds are gravitationally bound and roughly in virial equilibrium – we have examined this by looking at the sizes, virial parameters and virial masses for the cores. The virial mass of a core is the mass which a core of a given size and dispersion would have if in virial equilibrium (i.e. $2E_{\rm kinetic} = E_{\rm grav.\,potential}$). Assuming a spherical, unmagnetized cloud and a $\rho \propto r^{-2}$ density distribution, the virial mass, $M_{\rm vir}$, and virial parameter, α, are given by

$$M_{\rm vir} = \frac{\sigma_{\rm 3D}^2 R_{\rm eff}}{G}, \tag{12}$$

$$\alpha = \frac{R_{\rm eff}\sigma_{\rm 3D}^2}{G M_{850}} = \frac{M_{\rm vir}}{M_{850}}. \tag{13}$$

We use the masses based on the SLC 850 μm flux to calculate α, since $C^{18}O$ could be affected by depletion, particularly towards the most evolved starless cores. $R_{\rm eff}$ is the radius of the core as before, and $\sigma_{\rm 3D}$ is the three-dimensional velocity dispersion estimated from the one-dimensional $C^{18}O$ velocity FWHM (equation 8). Cores in virial equilibrium, $\alpha \approx 1$, and the size–virial parameter relation ($R_{\rm eff}$–α) will show no correlation. If $\alpha > 1$, the core is not gravitationally bound – it could dissipate or be in a pressure-confined state due to the surrounding gas. If $\alpha < 1$, the core cannot support itself against collapse, unless there are processes other than gravitation and turbulence involved.

We have examined the $R_{\rm eff}$–α relation in Orion A (Fig. 19b), which shows a large range in the virial parameter. The dotted line shows R against $1/R$. For the cores with the largest values of α, the $R_{\rm eff}$–α relation could be explained by the dependence of R and $1/R$. However, the majority of cores, both starless and protostellar, fall beneath this line. We find a medium strength anticorrelation between the virial parameter and the core size in the starless cores with $\rho = -0.61, P < 0.0001$. We do not detect a correlation for the protostellar cores, with $\rho = -0.27, P = 0.14$. As discussed previously, this may mean this relation ceases to hold for cores of the sizes 0.02–0.2 pc. The starless and protostellar cores do not form clearly separated populations – a Kolmogorov–Smirnov test on $R_{\rm eff}/\alpha$ cannot distinguish between the two samples.

Fig. 19(c) shows the relationship between $M_{\rm vir}$ and M_{850}. We find a strong correlation between these masses, with $\rho = 0.88, P < 0.0001$ for the protostellar cores and $\rho = 0.73, P < 0.0001$ for the starless cores. Objects following the Larson relations are expected to exhibit no strong correlation and be roughly centred on the $\alpha = 1$ line. We find a mean α values of 7.7 ± 12 (protostellar) and 14 ± 20 (starless). This also suggests that our cores are not following the Larson relation for the virial parameter.

From Figs 19(b) and (c), we can see that the larger cores in both size and mass appear more gravitationally bound than the smaller, less massive cores. It appears that the dominant effect in both of these measured relations is a strong correlation between the size and the mass. Comparing M_{850} and $R_{\rm eff}$, we find $\rho = 0.86$, $P < 0.0001$ for protostellar cores and $\rho = 0.89$, $P < 0.0001$ for starless cores, indicating a strong correlation between core mass and size. There is not a strong correlation between the size and the velocity dispersion within a clump.

The protostellar cores may belong to a different population than the starless cores. A Kolmogorov–Smirnov test on the M_{850} to $M_{\rm vir}$ ratio for protostellar and starless cores gives a low probability of 6.7×10^{-5}, suggesting they do come from different distributions. The starless cores have consistently lower SLC masses compared with their virial mass – indicating that the starless cores are more likely to be pressure confined by the cloud, rather than freely falling clumps.

It should be noted that we are making the assumption that our temperature estimations for the protostellar and starless cores are equally accurate. If there is a systematic difference in the true temperature compared with our estimate for either the protostellar or the starless population, then the differences that we see between the starless and protostellar SLC and virial masses could be partly due to differences in temperature. The presence of molecular outflows towards protostellar cores and the effect of their highly energetic motions on the dense cores is another factor that could influence the variation between the cores.

The Larson linewidth–size and size–virial parameter relations were originally found by showing a correlation between these properties for GMC and molecular cloud scale structures, and is commonly interpreted as being an effect of the supersonic turbulence in molecular clouds (McKee & Ostriker 2007). We do not see these

strong correlations and power laws for the Orion cores, suggesting that the turbulent motions are not the dominant factor determining these core properties at these size scales (0.02–0.2 pc). We also found that most of the cores are not gravitationally bound, suggesting that even the protostellar cores contain a significant component of unbound gas within them, presumably surrounding smaller, bound structures. However, we do note a potential bias in this analysis, since the emission from $C^{18}O$ we associate with a core may contain, or even be dominated by, 'intercore', or ambient, unbound gas, rather than the dense gas associated with star formation in the core. Further investigation will require both high-resolution IR classifications of protostellar sources in this region and high-resolution observations of chemical tracers of starless and pre-stellar cores.

6 SUMMARY

We have presented ^{13}CO and $C^{18}O$ $J = 3 \rightarrow 2$ data taken towards Orion A by the GBS, covering 5 pc of the filament including the OMC 1, OMC 2, OMC 3 and OMC 4 regions. In this section, we summarize the global properties of the Orion A cloud, the variation in cloud properties between cloud regions and the differences between cores with and without protostars.

It is well known that high-mass star formation occurs in the OMC 1 region, which contains BN–KL, the Orion nebula cluster and the Orion bar. The signatures are evident in the ^{13}CO and $C^{18}O$ properties. OMC 1 contains regions with significantly higher temperatures than average: towards the BN–KL region $T_{ex} \sim 58 \pm 4$ K, and towards the Orion bar $T_{ex} > 80$ K. The highest velocity dispersions are found towards OMC 1. It is the least optically thick region, with high $^{13}CO/C^{18}O$ intensity ratios observed towards regions of strong emission, consistent with a clumpy PDR structure. The OMC 1 outflows show the strongest emission in both isotopologues, suggesting that the protostars in OMC 1 are the most massive. (The Orion bar shows no evidence for outflows.)

Organic molecules characteristic of hot core chemistry, another tracer of high-mass star formation, are also well known towards OMC 1 core. In the passbands of $^{13}CO/C^{18}O$, we detect strong lines of CH_3CN, $^{13}CH_3OH$ and SO, and weaker lines of CH_3CHO, HC_3HO, CH_3OCHO, H_2CH_3HCN and $H_2{}^{13}CS$. These molecular lines are not detected anywhere else in Orion A, including the Orion bar, except for SO which is detected towards a second source, Orion-South, 1.5 arcmin south of the OMC 1 core.

The influence of earlier massive star formation on the Orion A cloud is also clearly seen in the H II region M43. This contains very little emission from either isotopologue, and the resulting emission cavity has a sharp spatial cut-off across the velocity range along the eastern wall, where the H II is expanding into the filament.

The reason behind the abundant, massive star formation in OMC 1 potentially lies in the massive filament that runs the entire length of the Orion A cloud. We consider the cloud to be a single, connected entity as a steady velocity gradient $\sim$1 km s^{-1} pc^{-1} runs along the filament from the northern OMC 3 to OMC 4 (though there is some evidence of a reversal in the region beyond OMC 4). A virial analysis based on filamentary cloud structure suggests that Orion A is too massive for thermal or turbulent support, but could be supported by magnetic fields. This is despite a high level of thermal support: the mean excitation temperature is 26 ± 4 K for ^{13}CO and 22 ± 6 K for $C^{18}O$. We calculate standard mass to virial mass ratios of 0.20 (0.27) for $C^{18}O$ (^{13}CO). This high ratio is consistent with the high level of star formation occurring throughout the filament. Using the corresponding critical value ratios for a magnetized filament leads to ratios $\gg$1, suggesting that a filamentary cloud model threaded by helical magnetic fields could be a model for Orion A. We measure a total gas mass of 4290 ± 89 M$_\odot$ for ^{13}CO, with 2420 ± 114 M$_\odot$ also detected over the smaller area of $C^{18}O$ emission.

Further considering the energy balance in the cloud, we look at the energy injected by molecular outflows. We detect a large number of outflows in ^{13}CO and we also detect high-velocity emission from $C^{18}O$ towards the most energetic of these. The detection of these rarer CO isotopologues indicates massive outflows which point to massive star formation, particularly in OMC 1. A lower limit of $\sim$3 per cent of the material traced by ^{13}CO is swept up and entrained in protostellar outflows. The energetic outflow activity traced by ^{13}CO produces 3.3×10^{40} J of kinetic energy across Orion A, comparable to the gravitational binding energy of the cloud, with similar amounts, $\sim$80 M$_\odot$, entrained in both the redshifted and blueshifted material. As many of the outflows are directed out of the filament, only a fraction of this energy will be deposited in the cloud, increasing levels of small-scale turbulence.

Subdividing the cloud regions into 0.1 pc scale cores based on sizes from a submillimetre dust core catalogue, we find there are more differences between cores in different parts of the cloud than there are between starless and protostellar cores (as classified on the basis of *Spitzer* data). Velocity dispersion and excitation temperature show no strong correlation with star formation but a clear increase from OMC 4 through OMC 2/3 to OMC 1. OMC 1 cores have a mean excitation temperature of 37.6 K and a distribution of velocity dispersions peaking at 0.66 km s^{-1}. The OMC 2/3 and OMC 4 regions have lower temperature cores, with means of 17.8 and 25.0 K, respectively, and velocity dispersions peaking at lower values, 0.47 and 0.38 km s^{-1}, respectively. Nonetheless, protostellar cores are, on average, more massive (even using a calculation based on T_{ex}) and have higher peak fluxes in both $C^{18}O$ and dust emission. There is a strong correlation between the mass derived from $C^{18}O$ emission and mass derived from 850 μm dust emission for all of the cores. The relationship can be fitted with a power law, with index 1.38 ± 0.17 for protostellar cores and 1.18 ± 0.11 for starless cores, the difference in the power-law indices being statistically insignificant. The power-law indices greater than 1 do suggest that both methods are proportional to the true mass within the cores, but there is a systematic difference which is larger at lower masses.

The cores do not follow the Larson size–linewidth relation, or show any other correlation between size and linewidth, which suggests that gravity dominates over turbulence on this size scale. The excitation temperatures for the high column density cores are similar [within a factor of 1.3 (1.4) using ^{13}CO ($C^{18}O$) emission] to those found using dust continuum observations, indicating that the excitation temperatures are a reasonable representation of the gas kinetic temperatures and the dust and gas are well mixed, as expected at densities of 10^4 H$_2$ cm^{-3}.

Based on the cloud properties above, a possible scenario for star formation in the Orion filament is that higher turbulent Jeans masses have led to the most massive and abundant star formation proceeding in OMC 1, followed by OMC 2/3, which contains the greatest fraction of protostellar cores and has the next highest excitation temperature and linewidth, with OMC 4 (which has the lowest linewidths) forming less massive cores and lower mass stars.

In future work, this data set will be compared with the spectral line data sets from other regions within the Gould Belt Survey to provide intercloud comparisons of physical characteristics and star-forming activity.

ACKNOWLEDGMENTS

The James Clerk Maxwell Telescope is operated by The Joint Astronomy Centre on behalf of the Science and Technology Facilities Council of the UK, the Netherlands Organisation for Scientific Research and the National Research Council of Canada. JFR acknowledges the support of the MICINN under grant number ESP2007-65812-C02-C01.

REFERENCES

Allen D. A., Burton M. G., 1993, Nat, 363, 54
André P., Ward-Thompson D., Motte F., 1996, A&A, 314, 625
André Ph. et al., 2010, A&A, 518, L102
Bally J., 2008, in Reiputh B., ed., Handbook of Star Forming Regions, Volume I: The Northern Sky. Astron. Soc. Pac., San Francisco, p. 459
Bally J., Langet W. D., Start A. A., Wilson R. W., 1987, ApJ, 312, L45
Bally J., Cunningham N., Moeckel N., Burton M. G., Smith N., Adam F., Nordlund A., 2011, ApJ, 727, 113
Bastien P., Jenness T., Molnar J., 2005, in Adamson A., Aspin C., Davis C. J., Fujiyoshi T., eds, ASP Conf. Ser. Vol. 343, Astronomical Polarimetry: Current Status and Future Directions. Astron. Soc. Pac., San Francisco, p. 69
Bergin E. A., Snell R. L., Goldsmith P. F., 1996, ApJ, 460, 343
Beuther H., Kramer C., Deiss B., Stutzki J., 2000, A&A, 362, 1109
Beuther H., Zhang Q., Greenhill L. J., 2005, ApJ, 632, 355
Blake G. A., Masson C. R., Phillips T. G., Sutton E. C., 1986, ApJS, 60, 357
Blake G. A., Sutton E. C., Masson C. R., Phillips T. G., 1987, ApJ, 315, 621
Buckle J. V. et al., 2009, MNRAS, 399, 1026
Buckle J. V. et al., 2010, MNRAS, 401, 204
Chernin L. M., Wright M., 1996, ApJ, 467, 676
Chini R., Reipurth B., Ward-Thompson D., Bally J., Nyman L.-A., Sievers A., Billawala Y., 1997, ApJ, 474, L135
Comito C., Schilke P., Phillips T. G., Lis D. C., Motte F., Mehringer D., 2005, ApJS, 156, 127
Conover W. J., 1998, Practical Nonparametric Statistics. Wiley, New York
Currie M. J., Draper P. W., Berry D. S., Jenness T., Cavanagh B., Economou F., 2008, in Argyle R. W., Bunclark P. S., Lewis J. R., eds, ASP Conf. Ser. Vol. 394, Astron. Data Analysis Software and Systems. Astron. Soc. Pac., San Francisco, p. 650
Curtis E. I., 2008, PhD thesis, Univ. Cambridge
Curtis E. I., Richer J. S., Buckle J. V., 2010, MNRAS, 401, 455
Davis C. J. et al., 2009, A&A, 496, 153
Davis C. J. et al., 2010, MNRAS, 405, 759
de Zeeuw P. T., Hoogerwerf R., de Bruijne J. H. J., Brown A. G. A., Blaauw A., 1999, AJ, 117, 354
Di Francesco J., Johnstone D., Kirk H., MacKenzie T., Ledwosinska E., 2008, ApJS, 175, 277
Dicker S. R. et al., 2009, ApJ, 705, 226
Fiege J. D., Pudtriz R. E., 2000, MNRAS, 311, 85
Frerking M. A., Langer W. D., Wilson R. W., 1982, ApJ, 262, 590
Garden R. P., Hayashi M., Hasegawa T., Gatley I., Kaifu N., 1991, ApJ, 374, 540
Genzel R., Stutzki J., 1989, ARA&A, 27, 41
Goddi C., Greenhill L. J., Humphreys E. M. L., Matthews L. D., Tan J. C., Chandler C. J., 2009, ApJ, 691, 1254
Goldsmith P. F., Bergin E. A., Lis D. C., 1997, ApJ, 491, 615
Goodman A. A., Barrance J. A., Wilner D. J., Heyer M. H., 1998, ApJ, 504, 223
Gould B. A., 1879, Resultados Obser. Nacional Argentino, 1, 1
Greaves J. S., White G. J., 1991, A&AS, 91, 237
Graves S. et al., 2010, MNRAS, 409, 1412
Hatchell J., Fuller G. A., Ladd E. F., 1999, A&A, 346, 584
Hatchell J., Richer J. S., Fuller G. A., Qualtrough C. J., Ladd E. F., Chnadler C. J., 2005, A&A, 440, 151
Henning T., Michel B., Stognienko R., 1995, Planet. Space Sci., 43, 1333
Heyer M. H., Brunt C. M., 2004, ApJ, 615, L45
Holland W. S. et al., 2006, in Zmuidzinas J., Holland W. S., Withington S., Duncan W.D., eds, Proc. SPIE Vol. 6275, SCUBA-2: A 10,000-pixel Submillimeter Camera for the James Clerk Maxwell Telescope. SPIE, Bellingham, p. 45
Jenness T., Cavanagh B., Economou F., Berry D. S., 2008, in Argyle R. W., Bunclark P. S., Lewis J. R., eds, ASP Conf. Ser. Vol. 394, Astronomical Data Analysis Software and Systems. Astron. Soc. Pac., San Francisco, p. 565
Jewell P. R., Hollis J. M., Lovas F. J., Snyder L. E., 1989, ApJS, 70, 883
Jijina J., Myers P. C., Adams F. C., 1999, ApJS, 125, 161
Johansson L. E. B. et al., 1984, A&A, 130, 227
Johnstone D., Bally J., 1999, ApJ, 510, L49
Johnstone D., Bally J., 2006, ApJ, 653, 383
Johnstone D., Boonman A. M. S., van Dishoeck E. F., 2003, A&A, 412, 157
Kawamura J. et al., 2002, A&A, 394, 271
Kim M. K. et al., 2008, PASJ, 60, 991
Kutner M. L., Ulich B. L., 1981, ApJ, 250, 341
Kutner M. L., Tucker K. D., Chin G., Thaddeus P., 1977, ApJ, 215, 521
Kwan J., Scoville N., 1976, ApJ, 210, L39
Ladd E. F., Fuller G. A., Deane J. R., 1998, ApJ, 495, 871
Larson R. B., 1981, MNRAS, 194, 809
Lee C. W., Cho S.-H., Lee S.-M., 2001, ApJ, 551, 333
Lee J.-E., Evans N. J., II, Shirley Y. L., Tatematsu K., 2003, ApJ, 583, 789
Lerate M. R. et al., 2006, MNRAS, 370, 597
Lis D. C., Serabyn E., Keene J., Dowell C. D., Benford D. J., Phillips T. G., Hunter T. R., Wang N., 1998, ApJ, 509, 299
McKee C. F., Ostriker E. C., 2007, ARA&A, 45, 565
Maddalena R. J., Morris M., Moscowitz J., Thaddeus P., 1986, ApJ, 303, 375
Menten K. M., Reid M. J., Forbrich J., Brunthaler A., 2007, A&A, 474, 515
Myers P. C., Linke R. A., Benson P. J., 1983, ApJ, 264, 517
Nutter D., Ward-Thompson D., 2007, MNRAS, 374, 1413
O'Dell C. R., Muench A., Smith N., Zapata L., 2008, in Reipurth B., ed., Handbook of Star Forming Regions, Volume I: The Northern Sky. Astron. Soc. Pac., San Francisco, p. 544
Olofsson A. O. H. et al., 2007, A&A, 476, 791
Onishi T., Mizuno A., Kawamura A., Ogawa H., Fukui Y., 1998, ApJ, 502, 296
Ostriker J., 1964, ApJ, 140, 1529
Persson C. M. et al., 2007, A&A, 476, 807
Peterson D., Megeath S. T., 2008, in Reipurth B., ed., Handbook of Star Forming Regions, Volume I: The Northern Sky. ASP Monographs, p. 590
Pineda J. E., Caselli P., Goodman A. A., 2008, ApJ, 679, 481
Plume R. et al., 2012, ApJ, 744, 28
Pöppel W. G. L., 2001, in Montmerle T., André P., eds, ASP Conf. Ser. Vol. 243, from Darkness to Light: Origin and Evolution of Young Stellar Clusters. Astron. Soc. Pac., San Francisco, p. 667
Sadavoy S. I. et al., 2010a, ApJ, 710, 1247
Sadavoy S. I., Di Francesco J., Johnstone D., 2010b, ApJ, 718, L32
Schilke P., Groesbeck T. D., Blake G. A., Phillips T. G., 1997, ApJS, 108, 301
Schilke P., Benford D. J., Hunter T. R., Lis D. C., Phillips T. G., 2001, ApJS, 132, 281
Serabyn E., Weisstein E. W., 1995, ApJ, 451, 238
Shirley Y. L., Huard T. L., Pontoppidan K. M., Wilner D. J., Stute A. M., Bieging J. H., Evans N. J., II, 2011, ApJ, 728, 143
Stanke T., McCaughrean M. J., Zinnecker H., 2002, A&A, 392, 239
Stognienko R., Henning T., Ossenkopf V., 1995, A&A, 296, 797
Sutton C., Blake G., Masson C., Phillips T. G., 1985, ApJS, 58, 341
Sutton E. C., Peng R., Danchi W. C., Jaminet P. A., Sandell G., Russell A. P. G., 1995, ApJS, 97, 455
Takami M. et al., 2002, ApJ, 566, 910
Tatematsu K., Kandori R., Umemoto T., Sekimoto Y., 2008, PASJ, 60, 407
Tedds J., Brand P. W. J. L., Burton M. G., 1999, MNRAS, 307, 337
Tercero B., Cernicharo J., Pardo J. R., Goicoechea J. R., 2010, A&A, 517, 96

Turner B. E., 1989, ApJS, 70, 539
Van Dishoeck E. F., Black J. H., 1988, ApJ, 334, 771
Ward-Thompson D. et al., 2007, PASP, 119, 855
White G. J., Padman R., 1991, Nat, 354, 511
White G. J., Sandell G., 1995, A&A, 299, 179
White G. J., Griffin M. J., Rainey R., Monteiro T. S., Richardson K. J., 1986, A&A, 162, 253
Williams J. P., Blitz L., Stark A. A., 1995, ApJ, 451, 252
Williams J. P., Blitz L., McKee C. F., 2000, in Mannings V., Boss A. P., Russell S. S., eds, Protostars and Planets IV. Univ. Arizona Press, Tucson, p. 97
Williams J. P., Plambeck R. L., Heyer M. H., 2003, ApJ, 591, 1025
Wilson T. L., 1999, Rep. Progress Phys., 62, 143
Wilson B. A., Dame T. M., Masheder M. R. W., Thaddeus P., 2005, ApJ, 430, 523
Wiseman J. J., Ho P. T. P., 1998, ApJ, 502, 676
Yoshida H., Phillips T. G., 2005, Proc. IAU Symp. 231, Astrochemistry: Recent Successes and Current Challenges. Poster Session, p. 245 http://adsabs.harvard.edu/abs/2005IAUS.235P.245Y
Yu K. C., Bally J, Devine D., 1997, ApJ, 485, L45
Yu K. C., Billawalla Y., Smith M. D., Bally J., Butner H. M., 2000, AJ, 120, 1974
Zielinsky M., Stutzki H., Störzer H., 2000, A&A, 358, 723
Ziurys L. M., McGonagle D., 1993, ApJS, 89, 155

This paper has been typeset from a TEX/LATEX file prepared by the author.